FIRST BROADBAND EXPERIMENTAL STUDY OF PLANAR THz WAVEGUIDES

By

RAJIND MENDIS

Bachelor of Science

University of Moratuwa

Moratuwa, Sri Lanka

1995

Submitted to the Faculty of the
Graduate College of the
Oklahoma State University
in partial fulfillment of
the requirements for
the Degree of
DOCTOR OF PHILOSOPHY
December, 2001

ACKNOWLEDGEMENTS

It is indeed with great pleasure that I extend my gratitude to Dr. Daniel R. Grischkowsky, my major advisor, for providing the opportunity to be a part of one of the best THz research groups in the world, and without whose scientific excellence and pioneering work in the THz field, this study would not have become a reality.

I also wish to thank the rest of my advisory committee, Dr. R. Alan Cheville, whose thirst for truth had me pondering over uncharted territory, Dr. James C. West, especially for the stimulating lectures in electromagnetics; the first person ever to get me to actively participate in a class room situation, and Dr. Albert T. Rosenberger, for imparting precise and clear understanding of numerous theoretical concepts in lasers and optics.

A very special thanks to Dr. Roger W. McGowan, probably the best experimentalist I have ever come across and who was a pleasure to work with, for teaching me many wonderful techniques in the laboratory.

I am also grateful to my colleague and good friend, John O'Hara, whose companionship alone, made the whole of Oklahoma State University an enjoyable place to be in; thank you, for bringing out the kid in me.

A heartfelt thanks to my parents, Ananda and Malini, for their love and support and for bringing me up to be the person that I am; I know that it wasn't the easiest thing on earth, and to my loving (adorable) wife Dilhara, for putting up with me and my *stuff*, and also for the confrontational task of proof-reading the final draft; you truly are a remarkable woman, and you make my life complete.

Finally, my appreciation goes to all human (and subhuman) elements not mentioned here, but whose contributions helped me succeed in this quest for knowledge.

TABLE OF CONTENTS

Chapter **Page**

LIST OF FIGURES

Figure **Page**

LIST OF SYMBOLS

b	Plate separation, m
c	Velocity of light in free-space, 3×10^8 m/s
C	Coupling coefficient
C_x	Coupling coefficient in x-direction
C_y	Coupling coefficient in y-direction
dc	direct current
d_p	Penetration depth of evanescent field, m
2-D	Two dimensional
E_{out}	Output electric field amplitude, V/m
E_{ref}	Reference electric field amplitude
E_y	Electric field amplitude in y-direction
E_z	Electric field amplitude in z-direction
f_{cm}	Cutoff frequency of m^{th}-order mode, Hz
FWHM	Full width at half maximum
GaAs	Gallium Arsenide
GVD	Group velocity dispersion
h	Half-thickness of dielectric slab, m
HDPE	High density polyethylene
H_x	Magnetic field amplitude in x-direction, A/m
IRS	Internal reflection spectroscopy

KLM	Kerr-lens mode-locked
L	Propagation length, m
m	Order of mode
$n_1 \sim n_3$	Refractive index
n_d	Refractive index of dielectric medium
N	Number of reflections
R	Characteristic resistance, Ω
R′	Configuration dependent parameter in loss equation
R'_f	Configuration dependent parameter associated with thin film
SOS	Silicon-on-sapphire
S_{wg}	Sensitivity of waveguide for thin film measurement
t	Thickness of thin film, m
t_e	Effective thickness of thin film
T	Transmission coefficient
TDS	Time-domain-spectroscopy
TEM	Transverse electric and magnetic
TE_1	First-order Transverse electric
Ti:Sapphire	Titanium: sapphire
TM_0	Zero-order Transverse magnetic
υ_g	Group velocity, m/s
υ_p	Phase velocity
$w1 \sim w3$	Beam waist
α	Amplitude absorption constant, cm^{-1}

α_f	Absorption constant of film medium
α_{yo}	Attenuation constant in y-direction in free-space, m^{-1}
β_o	Phase constant in free-space, rad/m
β_d	Phase constant in dielectric medium
β_{yd}	Phase constant in y-direction in dielectric medium
β_z	Phase constant in z-direction
Δh	Distance between true and fictitious boundaries, m
ε_o	Permittivity of free-space, 8.854×10^{-12} F/m
ε_d	Permittivity of dielectric medium
ε_r	Relative permittivity
ε_{rf}	Relative permittivity of film medium
η_o	Intrinsic impedance of free-space, 377 Ω
φ	Phase angle, rad
λ_o	Wavelength in free-space, m
λ_{cm}	Cutoff wavelength of m^{th}-order mode
μ_o	Permeability of free-space, $4\pi\times10^{-7}$ H/m
μ_d	Permeability of dielectric medium
θ	Incidence angle, degrees
θ_c	Critical angle
σ	Conductivity, S/m
ω	Angular frequency, rad/s

CHAPTER I

INTRODUCTION

The continued improvements in device performance and the demand for ever increasing bandwidth, will soon require the propagation of picosecond (ps) or subps pulses on micron or submicron sized wiring. This situation has forced the consideration of guided-wave propagation effects, for the interconnect between electronic chips and even down to the single chip level. Phenomena previously considered only by the microwave community at GHz frequencies are now becoming manifest in the ps time-scale at THz frequencies. An alternative to lithographically defined, high-bandwidth transmission lines on dielectric substrates is the guided-wave propagation of THz radiation, and the associated coupling between the guided and freely propagating THz beams. Recently, efficient broadband coupling of freely propagating ps pulses into hollow circular and rectangular metal waveguides [1,2], and single-crystal sapphire fibers [3], was demonstrated. Single-mode coupling and propagation were achieved for all these waveguides, even though for the metal waveguides the spectral bandwidth overlapped as many as 25 additional modes. Such waveguide propagation has already demonstrated much larger bandwidths with approximately 1/10th of the loss compared to that of lithographically defined coplanar transmission lines [4]. Although these waveguides are quite useful for narrowband or THz-TDS (time-domain-spectroscopy) applications, they all have very high group velocity dispersion (GVD), which render them incapable of subps pulse propagation. For the metal waveguides the excessive broadening of the pulses is caused by the extreme GVD near the cutoff frequency.

As stated in Reference [5], by specifically configuring a dielectric waveguide into the form of a thin slab (film) having a large aspect ratio, that is surrounded by loss-less dry air or vacuum, it is possible to reduce the attenuation constant by as much as 100 times below that of a similar circular dielectric rod with an identical cross-sectional area. The fact that the loss can be made so much smaller than that of an equivalent circular rod is primarily due to the distribution of the guided energy in the low-loss outer region. The distinguishing feature being its expanding surface area, which enables the guided mode to attach to it, quite unlike the case of the circular rod, which possesses minimal surface area. This simple waveguide structure can be fabricated using known low-loss dielectric materials, and can be made flexible to negotiate corners. It has been shown that this waveguide possesses rather stable behavior to dimensional variations, up to $0.1\lambda_o$ in surface roughness, where λ_o is the wavelength in free-space [6]. This dielectric slab waveguide also has good quasi-optic coupling properties, and is amenable to photolithographic techniques due to the planar geometry, thereby allowing active and passive devices to be integrated with the waveguide. In contrast to the previous work [1-3], the GVD can be controlled by the thickness of the slab, and the GVD can have a value opposite in sign to that of metal-tube or fiber waveguides, thereby allowing dispersion compensation or mutual pulse compression.

The first part of this dissertation presents an experimental study with a theoretical explanation, of single-mode propagation and quasi-optic coupling of ps THz pulses in dielectric slab waveguides [7]. Dispersive, low-loss propagation was observed within the bandwidth from 0.2 to 3.5 THz, for two slab waveguides made of high-density polyethylene (HDPE), having nominal dimensions of 150 μm (thick) by 10 mm (long), and 120 μm (thick) by 20 mm (long). The high GVD of the waveguides causes extensive pulse reshaping and broadening, resulting in positively chirped output pulses. The experiment and calculations based on the well-known 2-D waveguide model show that the linearly polarized (perpendicular to the plane of the slab) incoming THz beam couples significantly only to the dominant TM_0 mode resulting in predominantly single-mode propagation, even though the wideband input spectrum extends beyond the cutoff frequencies of several higher-order modes.

As demonstrated by this study, due to the prospect of achieving single-mode propagation with ultra low losses, the dielectric slab waveguide looks very promising for monochromatic or narrowband applications, and also for Guided-Wave THz-TDS discussed later in the dissertation. But unfortunately, the associated GVD hinders any possibility of undistorted subps pulse propagation, essential to high-speed data circuitry having data rates in the order of Tb/s.

The excessive pulse broadening due to GVD would not occur for the TEM mode of a two-wire coplanar line, a coaxial line, or a parallel-plate metal waveguide, that does not have a cutoff frequency. The signal velocities of such a TEM mode are determined solely by the surrounding dielectric medium. Quasi-optic coupling techniques would not be effective for the complex field pattern of the TEM mode of the two-wire coplanar line or the coaxial line. However, efficient coupling should be possible for the simple field pattern of the TEM mode of the parallel-plate metal waveguide.

The second part of this dissertation presents an experimental study with a theoretical explanation, of the parallel-plate waveguide, demonstrating efficient quasi-optic coupling of freely propagating subps pulses, and the subsequent low-loss, single

TEM mode propagation exhibiting virtually zero GVD [8]. Undistorted, low-loss propagation of input 0.3 ps FWHM pulses was observed within the bandwidth from 0.2 to 4 THz, for a parallel-plate copper waveguide having a plate separation of 108 μm and a propagation length of 24.4 mm. Consequently, for what is believed to be the first time, the ideal THz interconnect [4] that is capable of propagating subps pulses with minimal loss and no distortion has been realized. As an added feature of the parallel-plate waveguide, it is shown (theoretically) that the propagation loss could be reduced further, by using the opposite polarization and exciting the TE_1 mode, but at the expense of considerable GVD.

The third part of this dissertation is a supplement to the second part, where the concept of the parallel-plate waveguide has been extended to a very long, physically flexible, practicable THz interconnect having no GVD [9]. This study demonstrates the quasi-optic coupling and the subsequent low-loss, single TEM mode propagation of subps pulses in a parallel-plate copper waveguide, a quarter of a meter in length, that is bent in a plane normal to the plates, with the smallest bending radius being equal to 11.5 mm. Single TEM mode propagation is preserved as long as the axial changes in the waveguide (bends and twists) are spatially slow compared to the propagating wavelengths [10]. It is shown that the observed loss is mainly due to the finite conductivity of copper with some additional loss due to beam spreading in the unguided dimension. The observed pulse broadening is due to the frequency dependent loss since the GVD is negligible.

The last part of this dissertation is a purely theoretical study that focuses on deriving the far-infrared absorption spectra of very thin dielectric films using guided-wave techniques, substantiating a powerful THz technology, Guided-Wave THz-TDS. The dielectric film, which is coated on the surface of the dielectric slab waveguide or on the inner surface of the metal conductors of the parallel-plate waveguide, can be in the form of an adsorbed layer or a surface reaction. It is shown that for a propagation length of 2 cm, the sensitivity of a 50 μm thick dielectric slab waveguide that is made of high-resistivity silicon, can be as high as 400, when measuring the absorption of a film having an index of 1.5. Here, the sensitivity of the measurement is defined as the ratio of *absorption×length* product associated with the absorbing film on the waveguide surface to that of a single-pass transmission measurement at normal incidence of the free-standing film. For the same propagation length and film index, the sensitivity of a parallel-plate metal waveguide with a plate separation of 100 μm is shown to be 59.

CHAPTER II

BROADBAND THz SETUP

The experimental setup shown in Figure 2-1 consists of an optoelectronic transmitter and receiver, along with THz beam shaping and steering optics. As described in References [11] and [12], subps THz pulses are generated using 40 femtosecond optical pulses having a nominal wavelength of 820 nm, with a repetition rate of 100 MHz, from a KLM Ti:Sapphire laser. The optical pulses are focused onto the inner edge of the positive polarity line of a coplanar stripline on a semi-insulating GaAs wafer, which is biased at 70 V. Each pulse creates an electron-hole plasma, and the subsequent

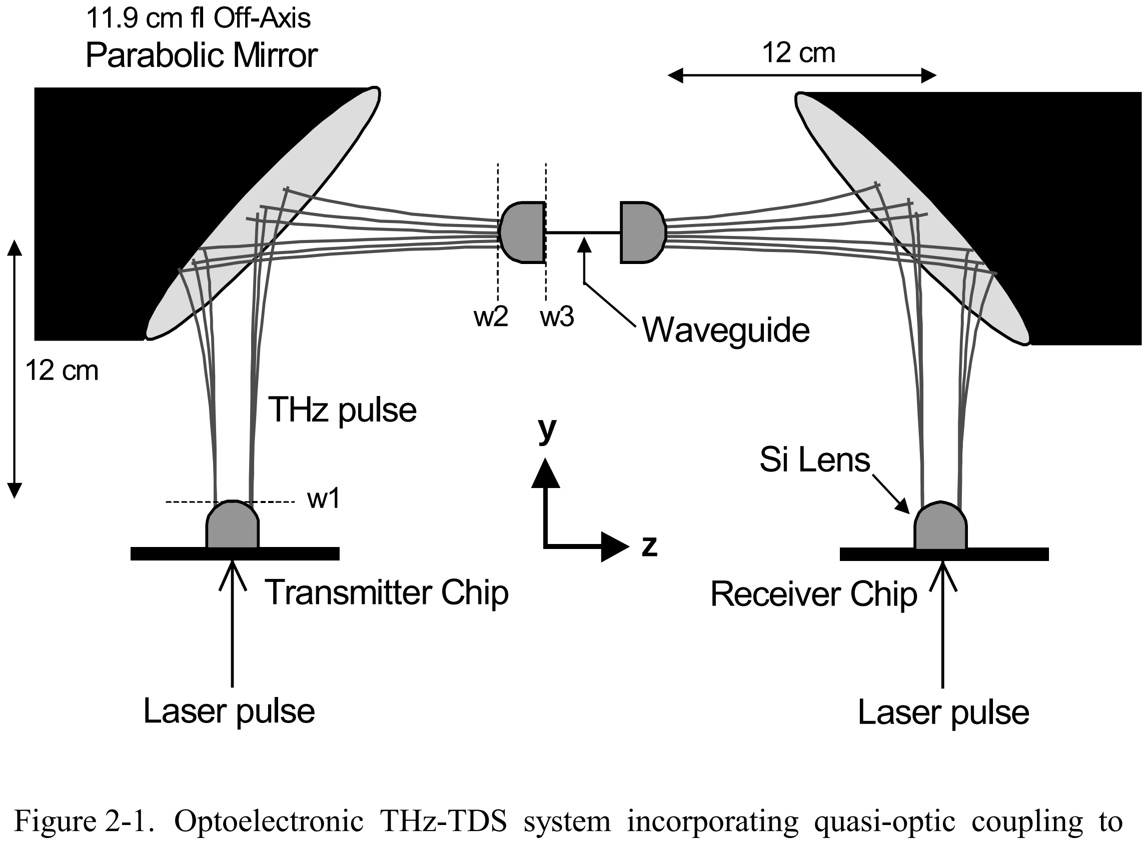

Figure 2-1. Optoelectronic THz-TDS system incorporating quasi-optic coupling to the waveguide. The generated THz pulse is linearly polarized in the plane of the paper and along the *y*-direction at the waveguide entrance face.

acceleration of these carriers by the bias field, generates a near single-cycle electromagnetic pulse of THz radiation, which would be linearly polarized along the direction of the bias field. In the standard THz-TDS setup, the sample under investigation is placed at the beam waist between the two off-axis parabolic mirrors, which are in the confocal configuration. The confocal symmetry gives a frequency-independent, unity power coupling efficiency for the optical system [13]. For the waveguide experiment presented here, a lens-waveguide-lens system is placed in this central position.

The transmitting antenna is at the focus of a hyper-hemispherical lens, made of high-resistivity silicon, which collimates the frequency-independent far-field pattern into a Gaussian beam with a $1/e$-amplitude waist diameter of 6 mm ($w1$). This waist is in the focal plane of the parabolic mirror, which focuses the beam to a second waist ($w2$), with beam diameters proportional to the wavelength (7.6 mm @ 1 THz). The combination of the parabolic mirror, silicon lens, and antenna chip constitutes the transmitter, the source of a highly directional, freely propagating beam of subps pulses. In the standard THz-TDS system, an identical optical system is on the receiver side, which is in fact the exact mirror image about the waist position $w2$. For the underlying waveguide experiment, an additional silicon lens, but with a plano-cylindrical geometry, is placed at waist $w2$, which focuses the beam further along one dimension. This gives rise to an approximately Gaussian beam having an elliptic cross-section whose frequency-dependent major axis is oriented parallel to the planar waveguide, and whose frequency-independent minor axis has a $1/e$-amplitude size of ≈ 200 μm at the focus ($w3$). This third focal plane is in the vicinity of the waveguide entrance face. A similar lens arrangement is used at the exit face as well. The first plano-cylindrical lens tightly couples the electromagnetic energy into the planar waveguide, and after propagation through the guide, the second lens tightly couples the energy out. In the absence of the waveguide, with the two cylindrical lenses moved closer such that their foci overlap, the system is again confocal, resulting in a frequency-independent coupling efficiency of unity. Even though not revealed in Figure 2-1, the beam at waist position $w2$ is effectively truncated to a diameter of 12 mm, by the holder of the cylindrical lens, which acts as a circular aperture.

At the receiver, the THz beam is focused onto a polarization sensitive, 10 μm dipole antenna on an ion-implanted silicon-on-sapphire (SOS) wafer, which is photoconductively switched by a second optical beam of 40 fs pulses from the same Ti:Sapphire laser. This generates a dc current that is proportional to the instantaneous value of the electric field of the propagated pulse. By measuring this current while scanning the relative time delay between the detected THz pulse and the gating optical pulse, the complete time-dependence of the THz pulse can be obtained, which includes both amplitude and phase information.

In order to eliminate effects of water vapor (there are significant water vapor absorption lines in the far-infrared region of the spectrum), the whole setup was enclosed in an air-tight enclosure and purged with dry air during data collection.

CHAPTER III

DIELECTRIC SLAB WAVEGUIDE

Waveguide Specimens

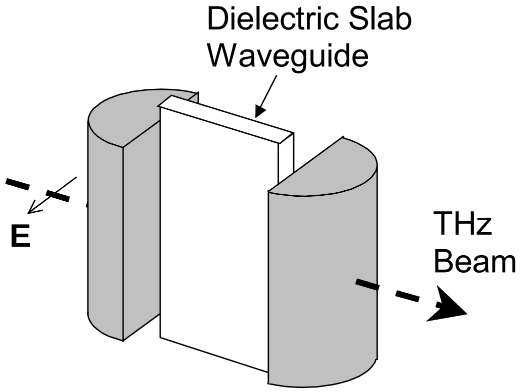

Figure 3-1. The lens-waveguide-lens system. The thickness of the dielectric slab has been exaggerated for clarity.

Two different dielectric slab waveguides that were fabricated in the laboratory, using commercially available sheets of HDPE having a refractive index of 1.5, were used in this experiment. The two waveguides had nominal dimensions of 150 μm (thick) by 10 mm (long) and 120 μm (thick) by 20 mm (long). The measured thickness of each waveguide varied by about ±10 μm along the plane of the slab. For both waveguides, the width in the lateral direction (*x*) was 20 mm.

Experimental Results

The reference pulse is obtained by removing the waveguide and moving the two cylindrical lenses closer, to their confocal configuration. Experimentally, this is done by maximizing the peak of the detected signal while bringing the two lenses closer in a step-by-step process, with precise alignment control. This reference pulse is effectively the input to the waveguide, except for a distinct phase delay corresponding to the propagation length of the guide. This pulse which has a positive peak of approximately 0.6 nA is shown in Figure 3-2 (a), with its amplitude spectrum in Figure 3-2 (b), that clearly shows a useful input spectrum extending from 0.1 THz to about 3.5 THz. The small oscillations seen after the main pulse in Figure 3-2 (a) are due to reflections within the small air-gap between the confocal lenses.

The measured propagated pulses through the 1 cm and 2 cm waveguides are shown in Figures 3-3 and 3-4, respectively, with their corresponding amplitude spectra. The incident THz pulse which has a full duration of about 1 ps, has been stretched to about 20 ps by the short waveguide and to about 40 ps by the long one. In addition to the larger spreading, the output of the long waveguide has a lot more oscillations than the output of the short one. And the leading portions of these two output pulses exhibit a positive chirp, where the high frequencies arrive later in time. This feature is completely opposite to what has been observed previously in other studies done on THz waveguides [1-3]. The trailing portions exhibit a slight interference effect. The stretching and consequent chirping of the propagated pulses compared to the incident pulse is attributed to the strong GVD of the waveguide.

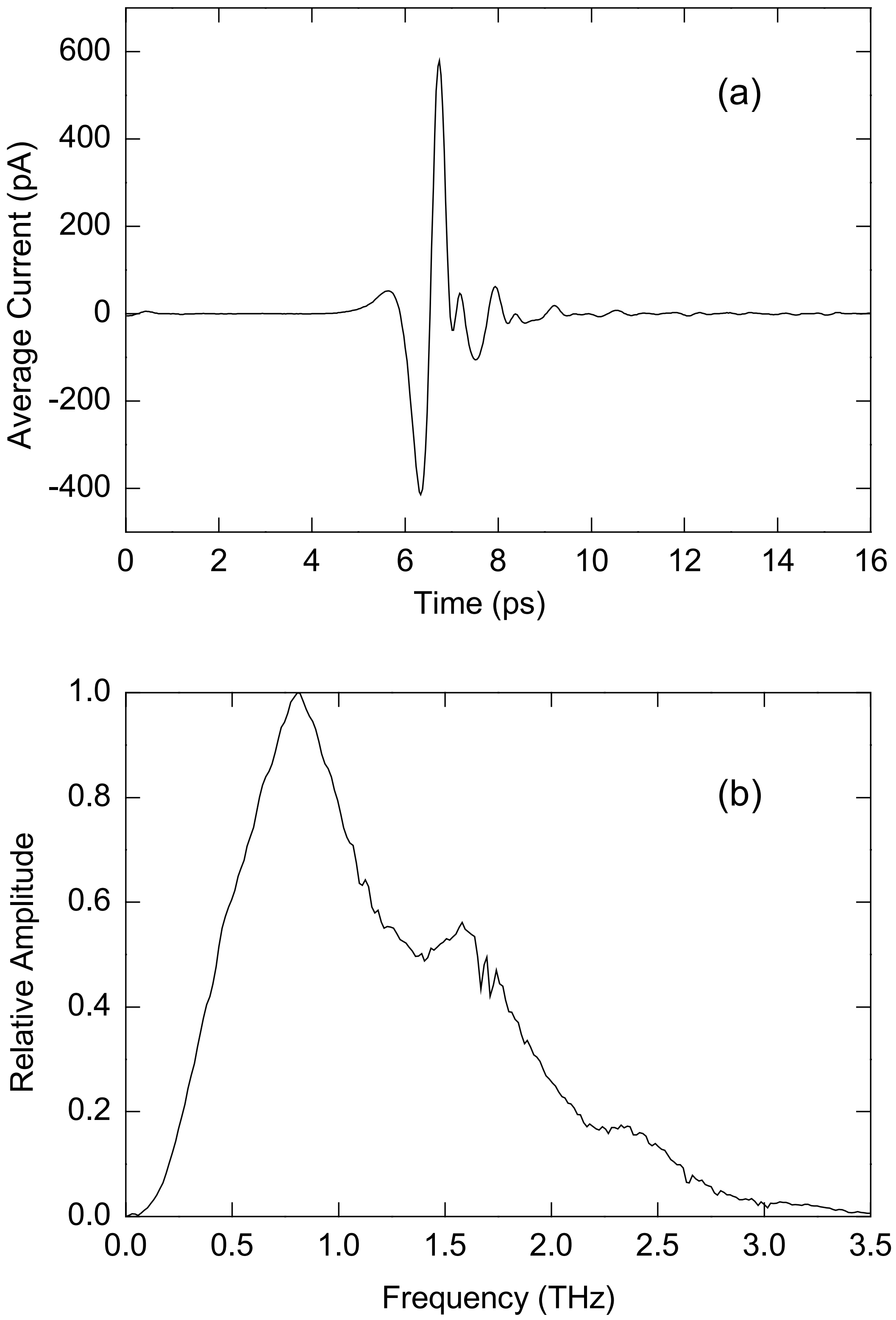

Figure 3-2. Measured reference pulse (a), and its amplitude spectrum (b).

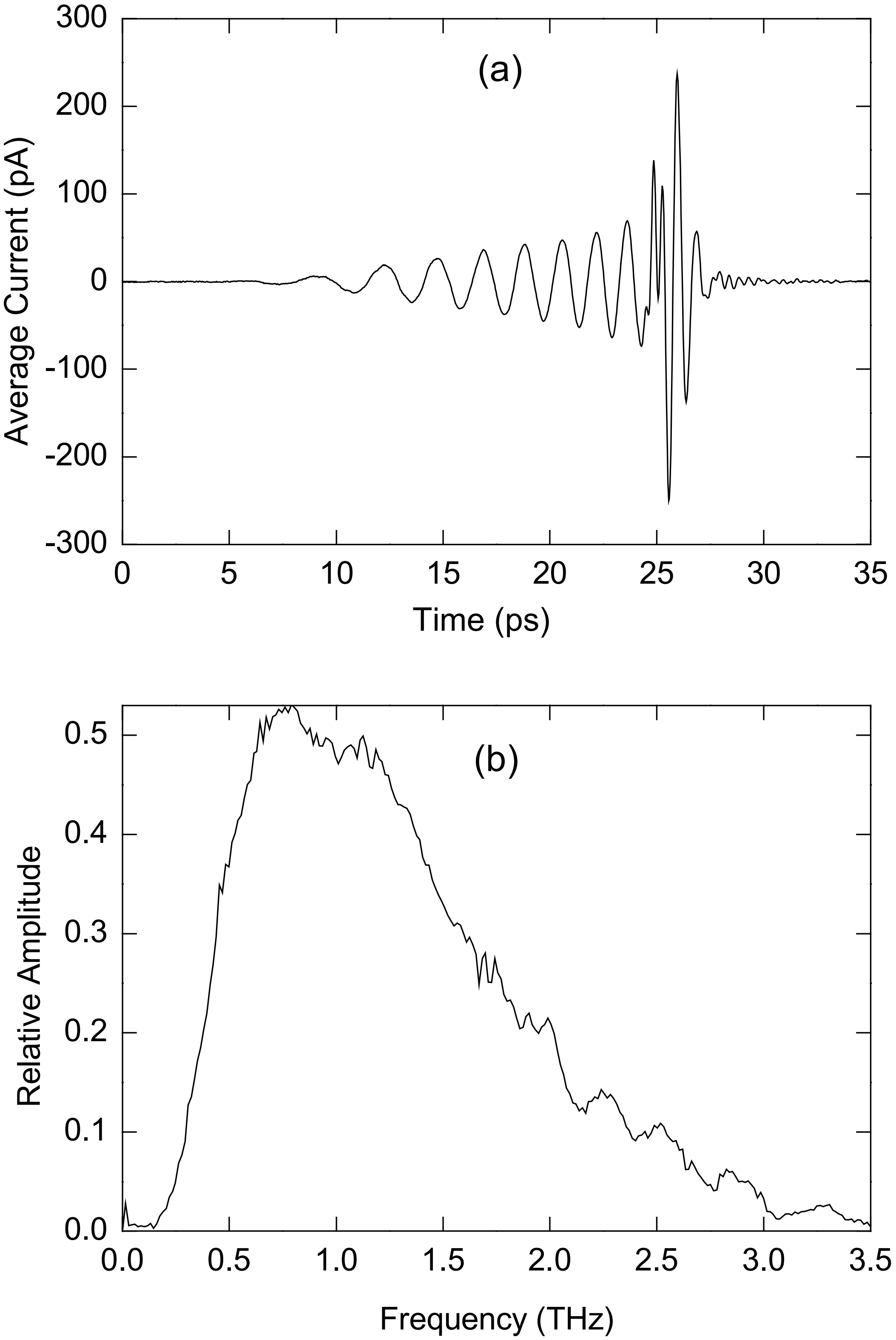

Figure 3-3. Measured propagated pulse through the short waveguide (a), and its amplitude spectrum (b).

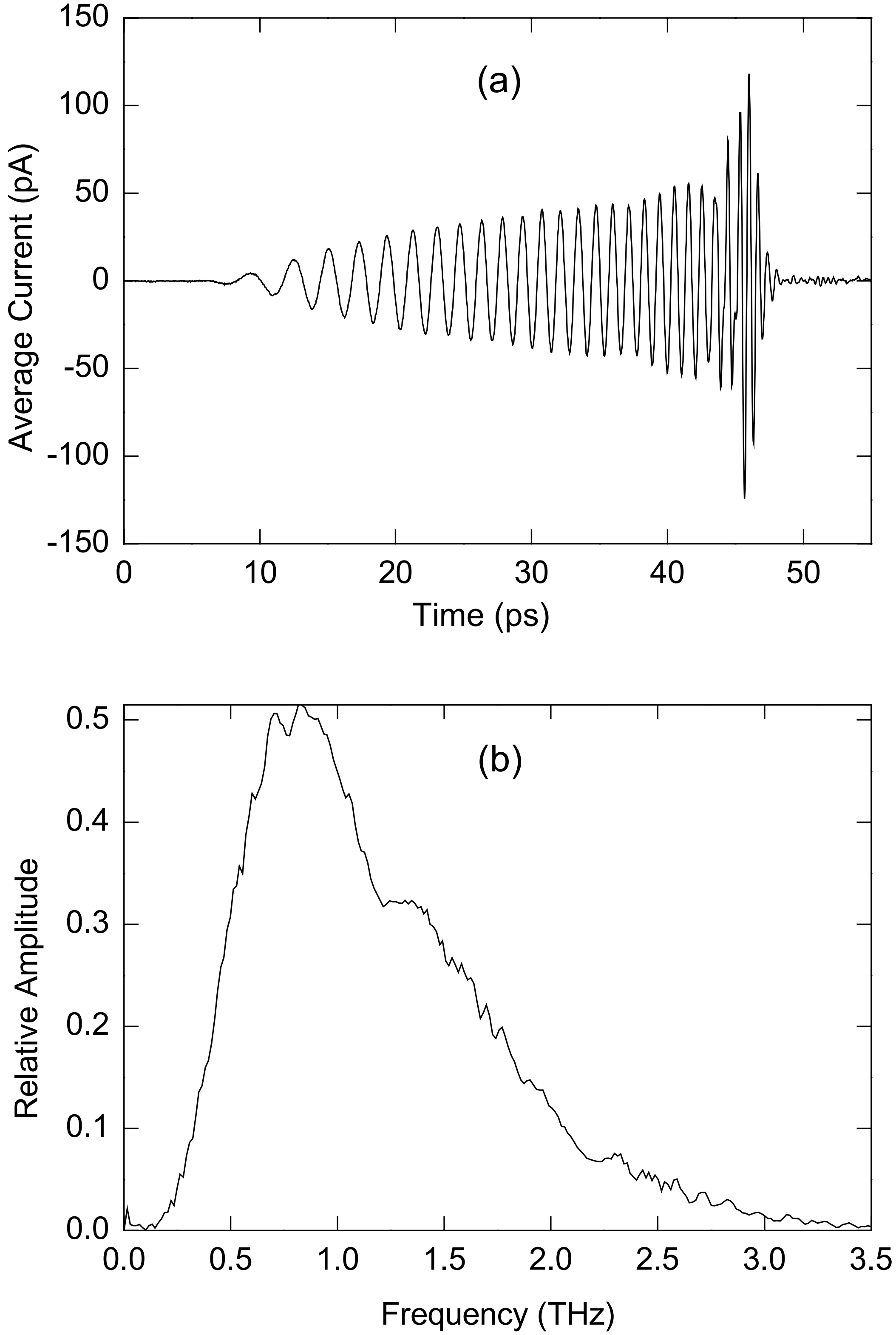

Figure 3-4. Measured propagated pulse through the long waveguide (a), and its amplitude spectrum (b).

Even though the amplitude spectra of the propagated pulses indicate a substantial loss in power compared to the spectrum of the reference pulse, a lot of useful energy is actually getting through, clearly exhibiting very efficient wave-guiding characteristics. This loss in signal level is mainly attributed to coupling losses at the entrance and exit faces of the waveguide, since the power absorption constant of HDPE is quite low, generally less than 1 cm^{-1} throughout the available spectrum.

It is also clear from the relatively smooth output spectra that there is no sharp low-frequency cutoff or any unusual oscillations (interference in the frequency domain due to multimode propagation) as observed in earlier investigations [1,2]. The smoothness in the amplitude spectra strongly implies dominant single-mode propagation through these planar waveguides, where the propagating mode has a cutoff frequency of zero.

Careful observation in the time domain indicates that the front-end of both output pulses arrive almost immediately after the arrival of the input reference pulse. This implies that the group velocity at the lower end of the spectrum is distributed very close to the velocity in free-space, for both waveguides.

Theoretical Analysis

The fundamental equation governing the input and output relationship of the system, assuming single-mode propagation, can be written in the frequency-domain as,

$$E_{out}(\omega) = E_{ref}(\omega) T C^2 e^{-j(\beta_z - \beta_o)L} e^{-\alpha L} \tag{3-1}$$

where $E_{out}(\omega)$ and $E_{ref}(\omega)$ represent the spectral components of the output and reference electric fields, respectively, T is the total transmission coefficient, C is the amplitude coupling coefficient, β_z is the phase constant, $\beta_o = 2\pi/\lambda_o$, α is the amplitude absorption constant, and L is the distance of propagation.

Modal Analysis

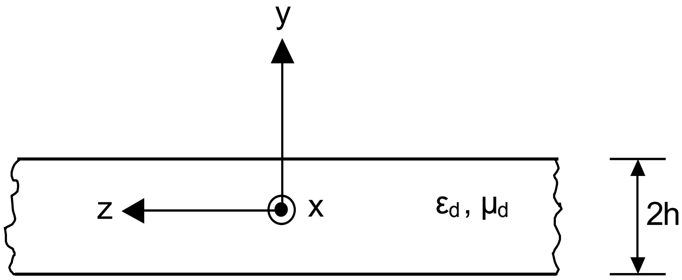

Figure 3-5. Longitudinal cross-section of the dielectric slab waveguide.

Based on the well-known slab waveguide model [14], for an input (Gaussian) electric field that is linearly polarized in a direction (y) normal to the plane of the dielectric slab, shown in Figure 3-5 as having a thickness of $2h$, only TM (odd) modes can exist in the waveguide. The non-vanishing terms of the field components (for a loss-less case) can be written as

$$-h \le y \le h, \qquad E_y = -\frac{\beta_{yd}\beta_z}{\omega\mu_d\varepsilon_d} A\cos(\beta_{yd}y)e^{-j\beta_z z}, \qquad E_z = -j\frac{\beta_{yd}^2}{\omega\mu_d\varepsilon_d} A\sin(\beta_{yd}y)e^{-j\beta_z z}$$

$$H_x = \frac{\beta_{yd}}{\mu_d} A\cos(\beta_{yd}y)e^{-j\beta_z z} \tag{3-2}$$

$$y \ge h, \qquad E_y = \frac{\alpha_{yo}\beta_z}{\omega\mu_o\varepsilon_o} B\, e^{-\alpha_{yo}y}e^{-j\beta_z z}, \qquad E_z = j\frac{\alpha_{yo}^2}{\omega\mu_o\varepsilon_o} B\, e^{-\alpha_{yo}y}e^{-j\beta_z z}$$

$$H_x = -\frac{\alpha_{yo}}{\mu_o} B\, e^{-\alpha_{yo}y}e^{-j\beta_z z} \tag{3-3}$$

$$y \le -h, \qquad E_y = \frac{\alpha_{yo}\beta_z}{\omega\mu_o\varepsilon_o} B\, e^{\alpha_{yo}y}e^{-j\beta_z z}, \qquad E_z = -j\frac{\alpha_{yo}^2}{\omega\mu_o\varepsilon_o} B\, e^{\alpha_{yo}y}e^{-j\beta_z z}$$

$$H_x = -\frac{\alpha_{yo}}{\mu_o} B\, e^{\alpha_{yo}y}e^{-j\beta_z z} \tag{3-4}$$

where $$\beta_{yd}^2 + \beta_z^2 = \beta_d^2 = \omega^2\mu_d\varepsilon_d \quad \text{and} \quad -\alpha_{yo}^2 + \beta_z^2 = \beta_o^2 = \omega^2\mu_o\varepsilon_o\,. \tag{3-5}$$

Here, subscript o stands for *free-space* quantities, and d stands for values *inside slab*. As commonly used, ω is the angular frequency, β is the phase constant, α is the attenuation constant (doesn't contribute to real power dissipation), ε is the permittivity, and μ is the permeability. A and B are two arbitrary constants which determine the absolute values of the fields.

The cutoff frequencies are given by

$$f_{cm} = \frac{mc}{4h\sqrt{\varepsilon_r - 1}}, \qquad m = 0, 2, 4, \ldots \tag{3-6}$$

where c is the velocity in free-space, and ε_r is the relative permittivity. The dominant mode is the TM$_0$ mode and its cutoff frequency is zero. It should be noted that the above analysis is carried out under the two-dimensional approximation, $\partial/\partial x = 0$.

Phase Constant

Application of boundary conditions yields the nonlinear transcendental equation [14]

$$\frac{\varepsilon_o}{\varepsilon_d}(\beta_{yd}h)\tan(\beta_{yd}h) = \alpha_{yo}h \tag{3-7}$$

which is used to numerically evaluate the phase constant β_z with the help of Equation (3-5) and the condition $\omega\sqrt{\mu_o\varepsilon_o} < \beta_z < \omega\sqrt{\mu_d\varepsilon_d}$.

Once the phase constant has been evaluated, the phase velocity (υ_p) and group velocity (υ_g) can be calculated as $\upsilon_p = \dfrac{\omega}{\beta}$, $\upsilon_g = \dfrac{\partial\omega}{\partial\beta}$.

Absorption Constant

The absorption associated with a dielectric waveguide having an axially uniform cross-section can be derived, by following Reference [15]. It is clear from this analysis that the absorption for a guided-mode can be written as

$$\alpha_{Guide} = \alpha_{Bulk}\sqrt{\varepsilon_r}R' \tag{3-8}$$

where α_{Bulk} is the absorption constant of the bulk dielectric material forming the waveguide, and the unitless quantity

$$R' = \frac{1}{\eta_o}\left|\frac{\int_{A_i}(\mathbf{E}\cdot\mathbf{E}^*)\,dA}{\int_{A_t}\hat{a}_z\cdot(\mathbf{E}\times\mathbf{H}^*)\,dA}\right|. \tag{3-9}$$

Here, η_o is the intrinsic impedance of free-space, A_i is the cross-sectional area of the core region, A_t is the total cross-sectional area (including the surrounding region of the guide), $\hat{a}_z$ is the unit vector in the direction of propagation, and **E** and **H** are the electric and magnetic field vectors of the guided-mode under consideration.

By choosing a desired configuration such as a slab (or film), the absorption can be drastically reduced [5]. Direct evaluation of R' using Equation (3-9) for the dominant TM$_0$ mode of the slab waveguide yields

$$R' = \frac{c}{2\omega\beta_z\varepsilon_r^2}\frac{\left[(\beta_z^2+\beta_{yd}^2)2h+(\beta_z^2-\beta_{yd}^2)\dfrac{\sin(2\beta_{yd}h)}{\beta_{yd}}\right]}{\left[\dfrac{1}{\alpha_{yo}}\cos^2(\beta_{yd}h)+\dfrac{1}{2\varepsilon_r}\left\{2h+\dfrac{\sin(2\beta_{yd}h)}{\beta_{yd}}\right\}\right]}. \tag{3-10}$$

Coupling & Transmission Coefficient

This calculation is done based on a quasi-optic picture assuming fundamental Gaussian beam propagation through the free-space paths. At the entrance face of the waveguide, a Gaussian beam is coupling onto waveguide modes. For single-mode propagation, at the exit face of the guide, the single guided-mode is coupling onto free-space Gaussian modes. Reciprocity of the system dictates an acceptance of only the fundamental Gaussian beam at the receiver. Due to this inherent symmetry, the amplitude coupling coefficient C is assumed to be the same at the input and output of the waveguide. The validity of these results is governed by the completeness and orthogonality of the respective modes [14,16].

The total transmission coefficient that takes into account the reflection losses (due to the impedance mismatch) at the input and output of the waveguide is given by

$$T = \frac{4\eta_p\eta_o}{(\eta_p+\eta_o)^2}, \tag{3-11}$$

where the wave impedance of the guided-mode is taken to be $\eta_p = \dfrac{\beta_z}{\omega \varepsilon_d}$.

The coupling coefficient is evaluated using the well-known overlap-integral [2]

$$C = \int_{A_t} (\mathbf{E}_i \cdot \mathbf{E}_p^*) \, dA , \tag{3-12}$$

where $\mathbf{E}_i$ and $\mathbf{E}_p$ represent the normalized electric field vectors of the Gaussian beam and the dominant guided-mode, respectively.

Comparison of Theory with Experiment

For the comparison, a thickness of 155 μm and a propagation length of 10.0 mm for the short waveguide, and a thickness of 116 μm and a length of 20.1 mm for the long waveguide, were used as the fitting parameters in the calculation. With respect to the actual dimensions of each waveguide, these are very realistic values. A constant (frequency-independent) refractive index of 1.5, was also used in the calculation, which is in good agreement with the negligible material dispersion (flat index) HDPE exhibits, all the way, into the far-infrared [17,18].

The complete theoretical propagation can be analyzed in terms of the dominant TM_0 (odd) waveguide mode, which has a zero cutoff frequency, as predicted by the experiment. Even though the wideband input spectrum extends beyond the cutoff frequency of the next higher-order (odd) mode permitted by the geometry of the waveguide (1.7 THz for the short one, and 2.3 THz for the long one), the output spectra do not reveal any significant multi-mode effects. This can be explained by the free-space to waveguide coupling, which is quite sensitive to the relative shape and the polarization of the beams. An elaborate discussion on this coupling aspect, with respective mode profiles, will follow later.

A notational confusion may arise from the above argument, which cites coupling from an *even* Gaussian beam to an *odd* waveguide mode. In the particular waveguide theory employed here [14], odd (or even) pertains to the magnetic vector potential, and not to the electric field amplitude. For the odd modes, the relevant electric field (in the y-direction) turns out to be even, since it is evaluated as the first derivative of the vector potential.

Phase & Group Velocity

The first step in the analytical process is the calculation of the phase constants derived separately from the measured data, and the underlying theory. Based on Equation (3-1), the experimental value of the phase constant β_z can be evaluated by taking the ratio of the phase spectra of the propagated and reference pulses. The plane wave nature of the input and output Gaussian beams at the entrance and exit faces of the waveguide does not allow any phase contribution from the product TC^2.

The theoretical value of β_z is numerically (iteratively) evaluated at each frequency, using Equations (3-7) and (3-5), as explained earlier. In general, at high frequencies, the transcendental equation (3-7) may have more than one solution (implying the possibility of higher-order modes), within the range stipulated by the inequality condition. When this occurs, the appropriate value for the lowest order dominant mode is found to be the one having the largest value, in accordance with Equation (3-5).

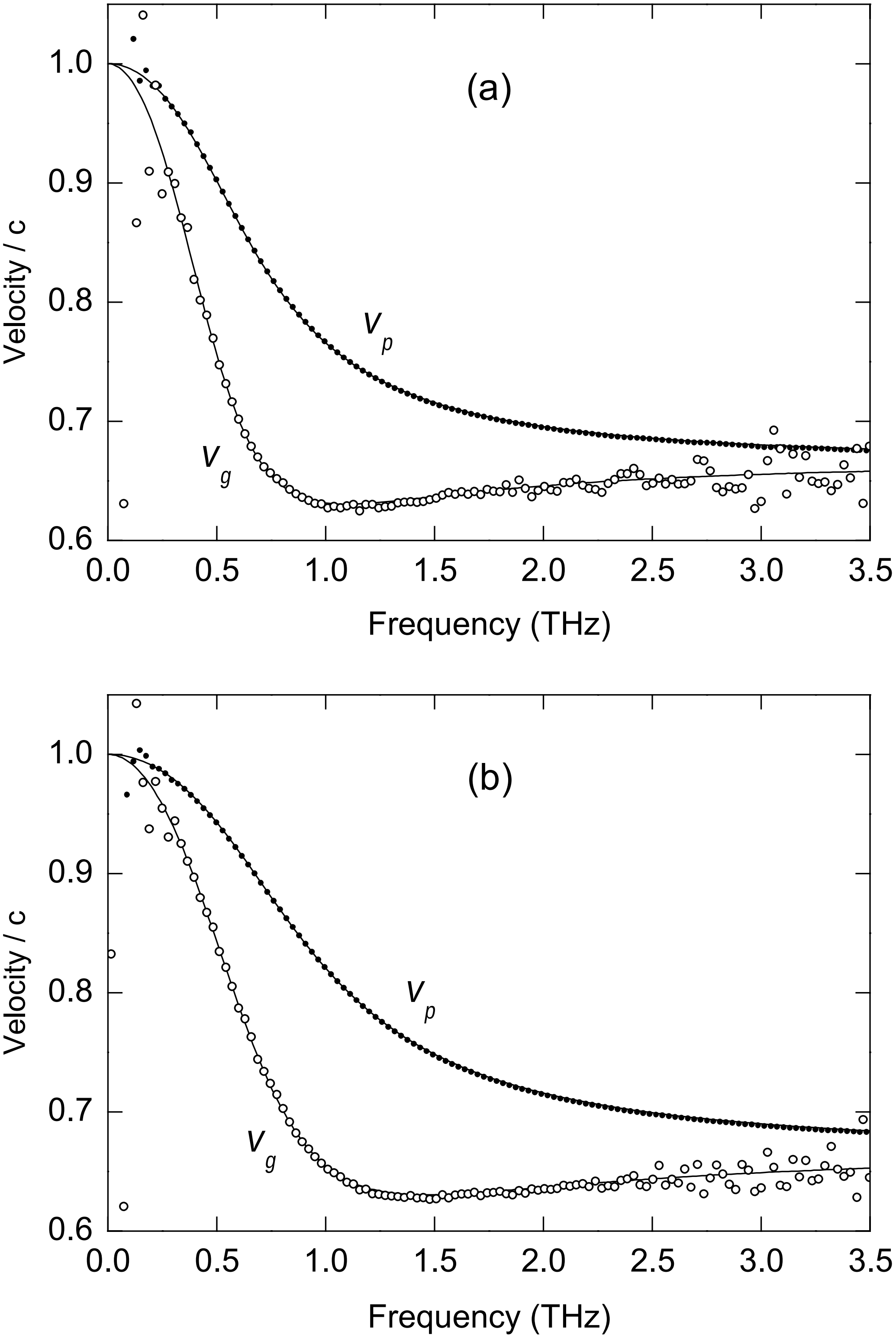

Figure 3-6. Theoretical and experimental values of the phase velocity and group velocity for the short (thick) waveguide (a), and the long (thin) waveguide (b). The dots and the open circles correspond to the experimental values.

The theoretical and experimental values of υ_p and υ_g derived using β_z, are plotted (as a ratio with respect to *c*) in Figures 3-6 (a) and (b) for the short and long waveguides, respectively. It can be clearly observed that the velocities approach that of bulk polyethylene at the high frequencies, while at the very low frequency end they approach that of free-space. This changeover is due to the spatial power flow of the waveguide changing from containment within the core region at high frequencies, to a surface-guided wave traveling in the free-space region at low frequencies. Most of the GVD is seen to occur towards the low frequency part of the spectrum, up to about 1 THz for the short and thick waveguide [Figure 3-6 (a)], and up to about 1.4 THz for the long and thin one [Figure 3-6 (b)]. This highly dispersive region corresponds to a positive chirp in the time-domain, where υ_g decreases as the frequency increases. The wider range for the thin one would generally imply that if the waveguides were of the same length, the thin one would cause more oscillations in the time-domain, than the thick one.

At the low-frequency limit υ_g is very close to *c*, explaining the almost immediate arrival of the propagated pulses with respect to the arrival of the reference pulse. An interesting feature in the υ_g plot is the presence of a well-defined minimum region with zero GVD, which conveys the possibility of two different frequency components on either side of the minimum, propagating with the same υ_g, which in turn would give rise to an interference effect among different frequency components in the time domain. This interference (in the same mode) is exclusive to the time-domain, and will not be present in the amplitude spectra. Furthermore, the minimum points (which correspond to the frequencies having the lowest velocities) for both the thick (short) and thin (long) waveguides, are at relatively the same level, and implies that pulse broadening would be more or less the same, if the waveguides were of the same length.

As can be seen by the comparison, there is excellent agreement between theory and experiment. The noise present in the group velocity plots, at the high frequency end and at the extreme low frequency end, is caused by the inherent enhancement in taking the first derivative.

Mode Profile

The mode profile of the guided-mode can be derived once β_z is known, using Equations (3-2) to (3-5). This, expressed in terms of the magnitude variation of the key component of the electric field (E_y), is frequency dependent as shown in Figure 3-7, which illustrates that associated with the short waveguide. In particular, this is the normalized electric field in the y-direction, evaluated at points located along the y-axis, at an arbitrary cross-section of the waveguide, where the origin of the x-y plane is at the centroid of the cross-section.

Figures 3-7 (a)-(d), correspond to the frequencies, 0.3, 0.6, 1, and 2 THz, respectively. The changeover in the spatial power flow, going from a surface-guided mode at low frequencies to a fully confined mode at high frequencies, is clearly seen from this diagram. Due to the boundary conditions at the slab surfaces, where the electric field is normal to the air-dielectric interface, there is a discontinuity in the field amplitude corresponding to a factor of ε_r.

Quasi-optic Coupling

The coupling can be understood in terms of a modal expansion of the input

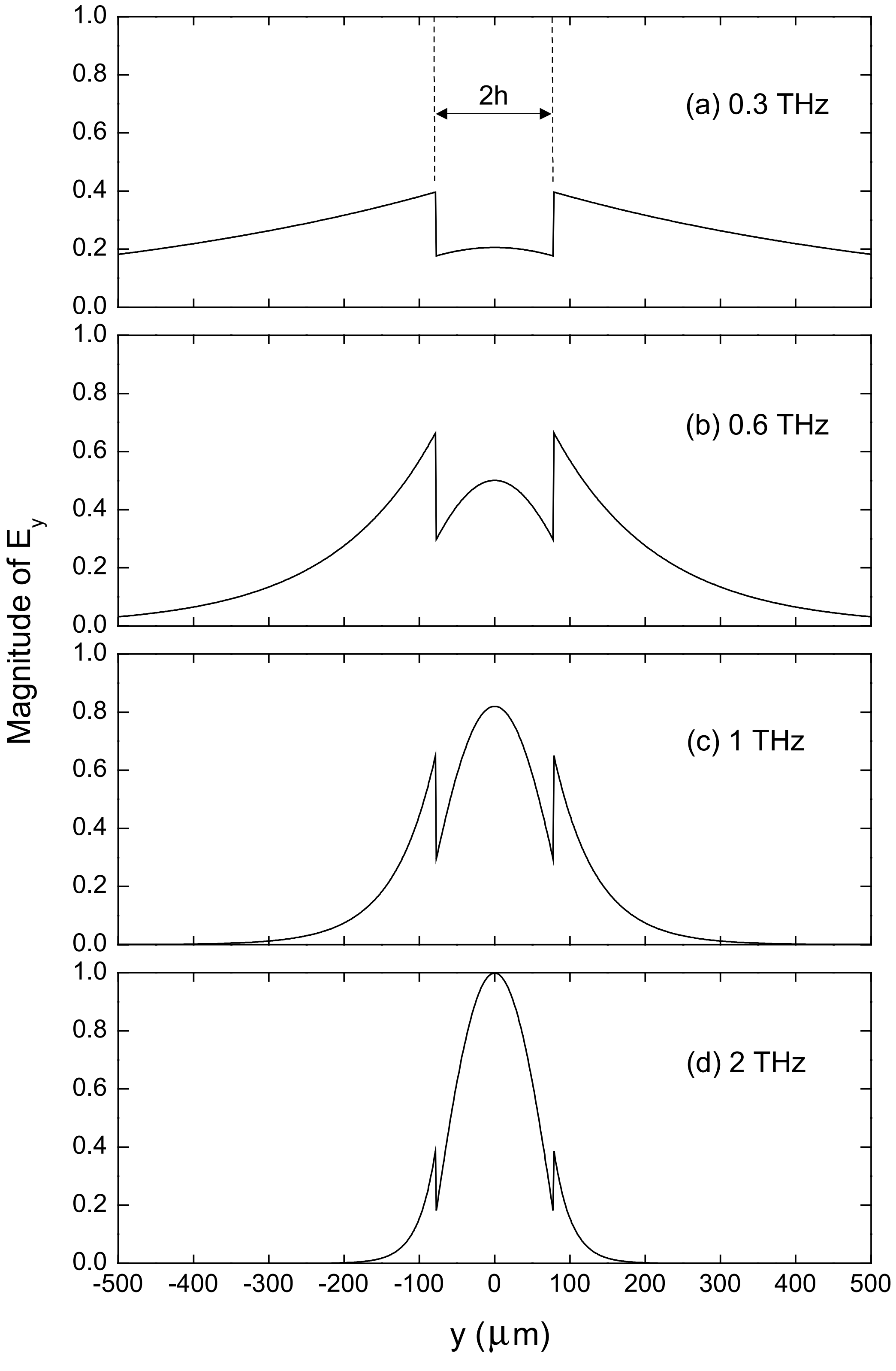

Figure 3-7. Mode profiles corresponding to the frequencies, 0.3 THz (a), 0.6 THz (b), 1 THz (c), and 2 THz (d), derived for the short waveguide. The discontinuity corresponds to the dielectric-air interface.

tangential field, where the field can be uniquely represented by a summation over the eigen-modes that form a complete basis set [19]. In general, for the planar dielectric waveguide, in addition to the discrete spectrum of guided-modes, a continuous spectrum of radiation modes is also required for completeness [16]. But here (and in almost all other literature) radiation modes are not included for simplicity [20,21]. Radiation modes do not play a significant role when almost all of the power is coupled into the guided-modes. A complete set of guided-modes is formed by the two generic classes referred to as TM (transverse magnetic to the direction of propagation) and TE (transverse electric to the direction of propagation). Each class is further divided into Odd and Even groups based on the functional symmetry of their vector potentials.

The experiment demands an even E_y component, making propagation possible only for the TM (odd) modes. And due to the orthogonality of these guided-modes, the coupling coefficients can be derived by the calculation of the overlap-integral as described in Equation (3-12). It should be noted that the entire analysis uses a two-dimensional model, which implicitly assumes a Gaussian profile in the x-direction for the guided-mode fields, in the coupling calculation. The two-dimensional approximation is justified because there are no restrictions (boundary conditions) to the field along the x-direction [22].

As mentioned earlier, the geometry of the waveguides used in the experiment, actually permits the propagation of two TM (odd) modes, the dominant mode with a zero cutoff frequency, and the next higher-order mode with a cutoff at 1.7 THz for the short one, and at 2.3 THz for the long one. But, the experimental results suggest a predominantly single-mode propagation. A qualitative explanation to this can be given using Figure 3-7. It was stated earlier that any input field could be uniquely represented by a combination of the waveguide modes. It is understood that these modes are excited to match the input beam in space and in time (at the entrance to the waveguide). The incident beam has a Gaussian profile that matches well with the guided-mode profile at sufficiently high frequencies [Figure 3-7 (d)]. As the frequency gets lower, the guided-mode profile starts to deviate considerably from a Gaussian, and the mismatch becomes more and more prominent. This is apparent going from Figures 3-7 (d) to (a). Therefore, at low frequencies more modes are required for matching. But, at the same time, the waveguide doesn't allow any higher-order modes to propagate below 1.7 THz for the short waveguide, and 2.3 THz for the long one. And therefore, a predominantly single-mode propagation prevails. There may be a slight trace (of the next higher-order mode) going through, which compensates for the mismatch at high frequencies. If present at all, this leakage will be greater for the short waveguide. The modes that are excited, but not allowed to propagate (below cutoff), will radiate from the sides of the guide at the vicinity of the excitation point.

Even though previous studies have emphasized coupling of the Gaussian input to the waveguide to be at the exact waist of the input beam, thorough investigations reveal that a slight shift (of the waveguide face) from the waist position gives much better overall coupling throughout the spectrum. This new finding is attributed to the frequency dependent nature of the spatial mode profiles, in contrast to the modes of metal waveguides. Slightly away from the waist position, the size of the minor axis of the elliptic-Gaussian beam (which is frequency independent at the waist) increases with decreasing frequency, accommodating the expanding field of the guided-mode.

Most of the above arguments will also hold at the exit face of the waveguide, the only difference being that coupling is from the (single) guided-mode to free-space Gaussian modes. Due to reciprocity, only the fundamental Gaussian mode will be accepted by the receiver, which results in an almost identical situation at the exit face.

Absorption

If the power absorption constant of the bulk dielectric material is known, the loss due to absorption by the waveguide can be calculated using Equations (3-8) and (3-10). But, obtaining the exact absorption (in the THz frequency range) of processed polyethylene is not a simple task, given the inherent specimen dependence (variations from sample to sample). Impurities acquired during the manufacturing process play a significant role in the actual absorption. Therefore, it was deemed necessary to derive the absorption of the bulk material, also using the results of the experiment, in order to carry out a final comparison of the measured propagated pulse with a theoretical one (where the reference pulse is subjected to a theoretical propagation through the waveguide).

Since there are two sets of data (for the two guides) and all the waveguide parameters except the absorption is known, one set of data can be used to derive the absorption, which in turn can be used on the other set to carry out the calculation in the time-domain. This method of deriving the bulk absorption assumes a very pure spectral analysis using the relevant amplitude spectra, which can be contaminated by any multi-mode effects. Therefore, the data set of the long waveguide, which has the least probability of contamination (due to less leakage), was used for the absorption calculation. And this value, which was found to be reasonably consistent with published

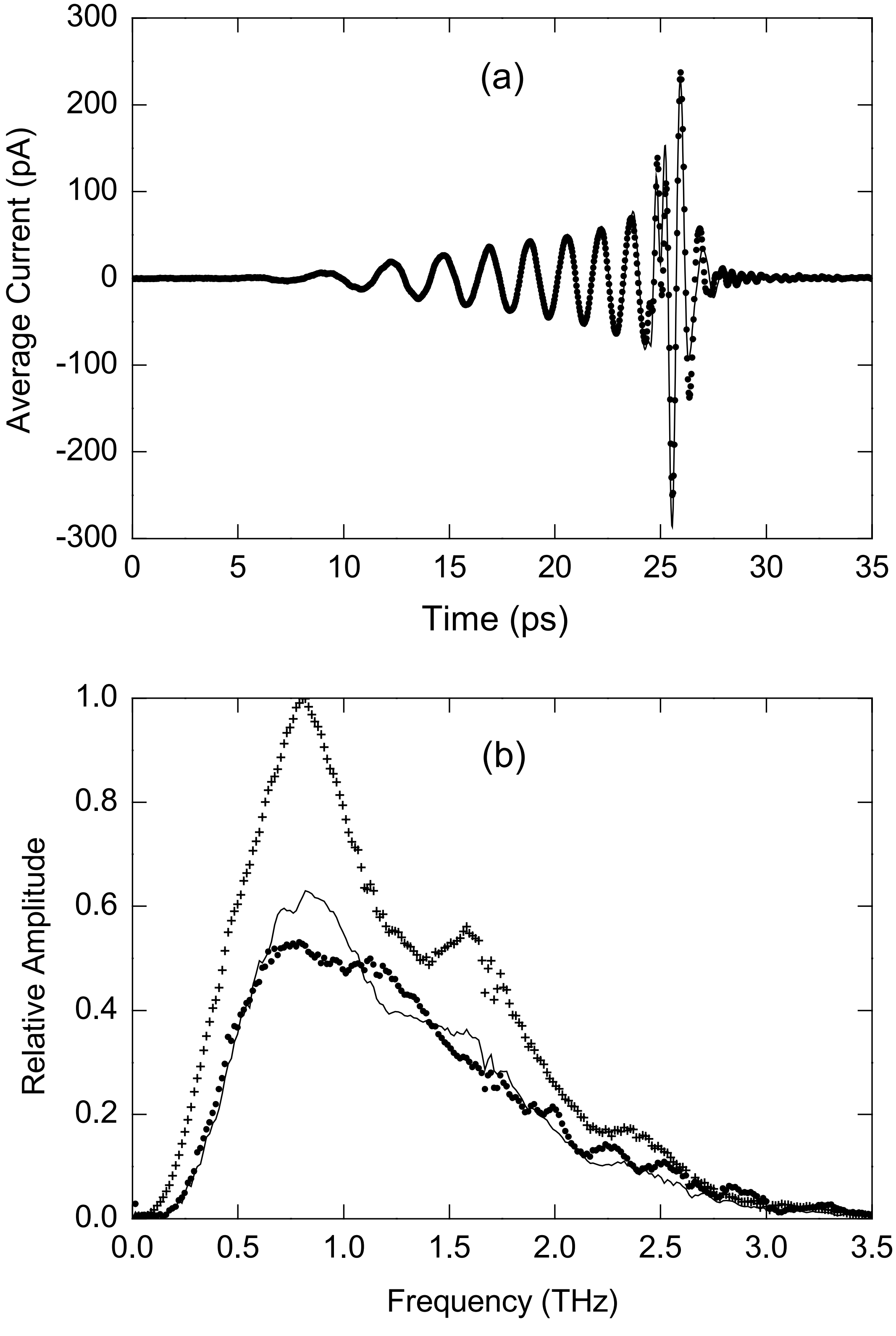

Figure 3-8. Measured (dots) and theoretically predicted (solid line) propagated pulses through the short waveguide (a), and the corresponding amplitude spectra (b). Amplitude spectrum of the reference pulse (crosses) is also shown in (b).

[17,18,23] and unpublished results, was used on the short waveguide data to derive the theoretically propagated pulse. In calculating the propagated pulse, the time-domain reference pulse was transformed into the frequency-domain (by taking the Fourier Transform), where all the propagation and coupling parameters had been evaluated for the short (thick) waveguide. Substituting in Equation (3-1), and transforming back into the time-domain (by taking the Inverse Fourier Transform), leads to the calculated output waveform. This final comparison shown in Figure 3-8 (a) with the corresponding amplitude spectra in Figure 3-8 (b), clearly shows excellent agreement between theory and experiment, in keeping with any inaccuracies that may have come into play during the experimental procedure.

CHAPTER IV

PARALLEL-PLATE WAVEGUIDE

Waveguide Specimens

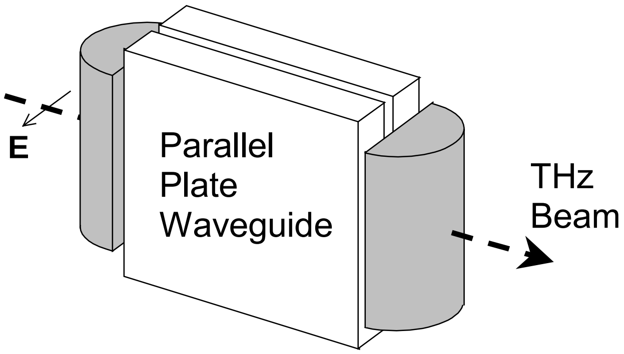

Figure 4-1. The lens-waveguide-lens system. The plate separation has been exaggerated for clarity.

As shown in Figure 4-1, the waveguide consists of two parallel conducting plates positioned close together to form the guide. In this experiment the gap between the plates was air-filled, even though in general, it can be filled with any dielectric material. The metal plates were machined using commercially available copper having an electrical conductivity of 5.76×10^7 S/m. The inner surfaces as well as the side surfaces forming the input and output faces of the waveguide were polished using 1500 grit finishing sheets. A 108 μm separation was provided by two dielectric strips sandwiched between the plates at the top and bottom. This provided an air-duct having cross-sectional dimensions of 108 μm (thick) by 15 mm (wide). Since the lateral width of the beam was smaller than 15 mm, it was guaranteed that the guide acted in a manner similar to a parallel-plate waveguide. Two waveguides, differing in length were fabricated in this manner, one 12.6 mm long and the other 24.4 mm long.

The cylindrical lenses used were different from the earlier experiment, with a much larger focal length (≈ 0.75 mm from the flat surface). These were used to provide a larger delay to the reflections, allowing artificial removal of the reflections from the main pulse, in order to clean up the amplitude spectra.

Experimental Results

As before, the reference input pulse is obtained by removing the waveguide and moving the cylindrical lenses to their confocal position. This pulse which has a positive peak of approximately 0.5 nA and a FWHM of about 0.3 ps is shown in Figure 4-2 (a). The small secondary pulse seen after a delay of about 10 ps is due to the reflections from the flat surfaces of the two lenses. The propagated pulses through the 12.6 mm long and the 24.4 mm long parallel-plate waveguides are shown in Figures 4-2 (b) and (c), respectively. The secondary pulses are due to the reflections at the input and output of the waveguides. Even though the wave impedance is the same for the freely propagating Gaussian beam and the guided mode, the reflections at the input and output faces of the waveguide (in addition to the reflections from the flat surfaces of the lenses) are due to the mismatch in the size (especially at low frequencies) of the freely propagating beam and the guided mode at the coupling plane. Each secondary pulse, seen after the main propagated pulse, is in fact the result of two pulses (created at the two ends of the waveguide) overlapping in time.

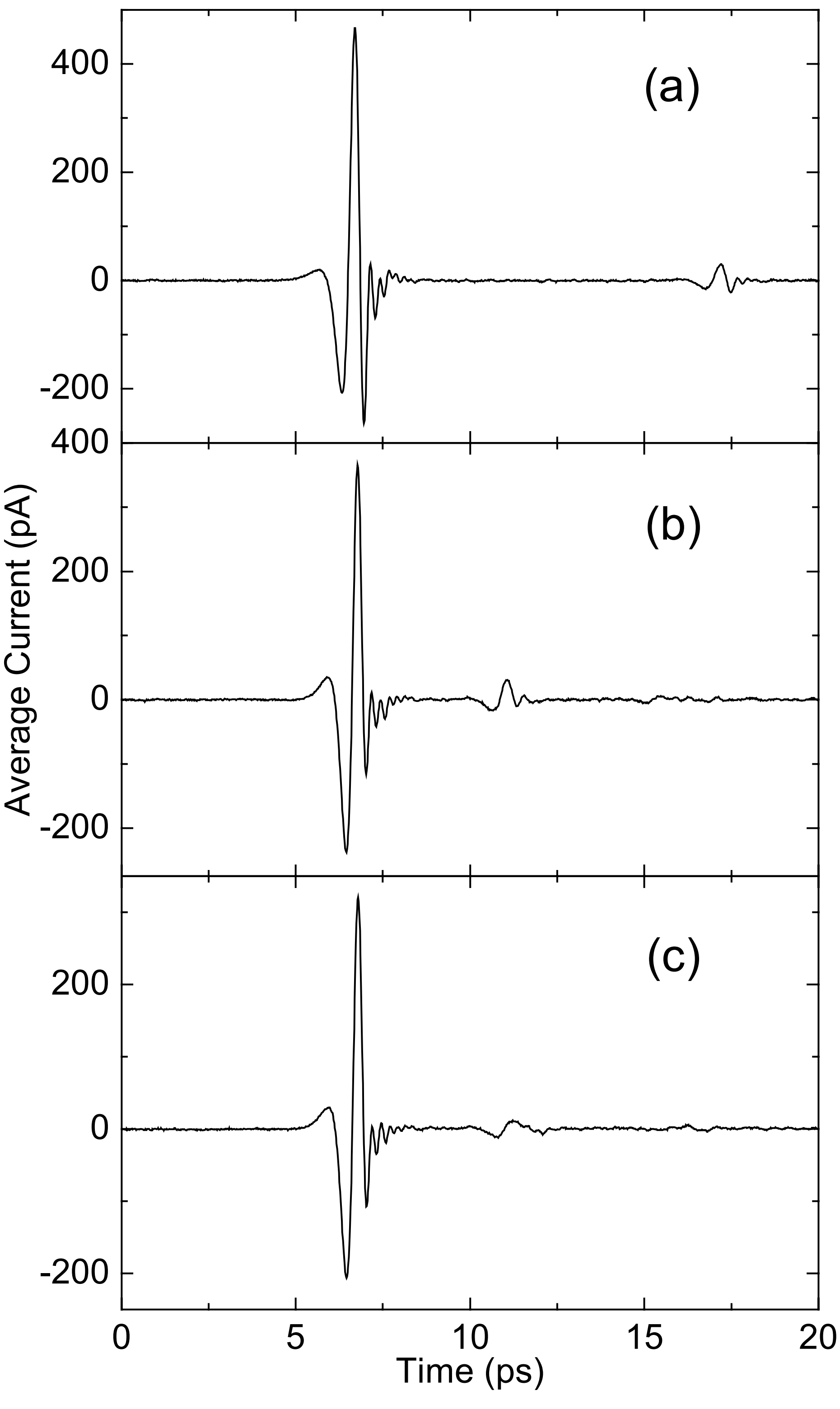

Figure 4-2. Scans of the reference pulse (a), the propagated pulse through the short waveguide (b), and the propagated pulse through the long waveguide (c). The zero reference time is the same for (a)-(c).

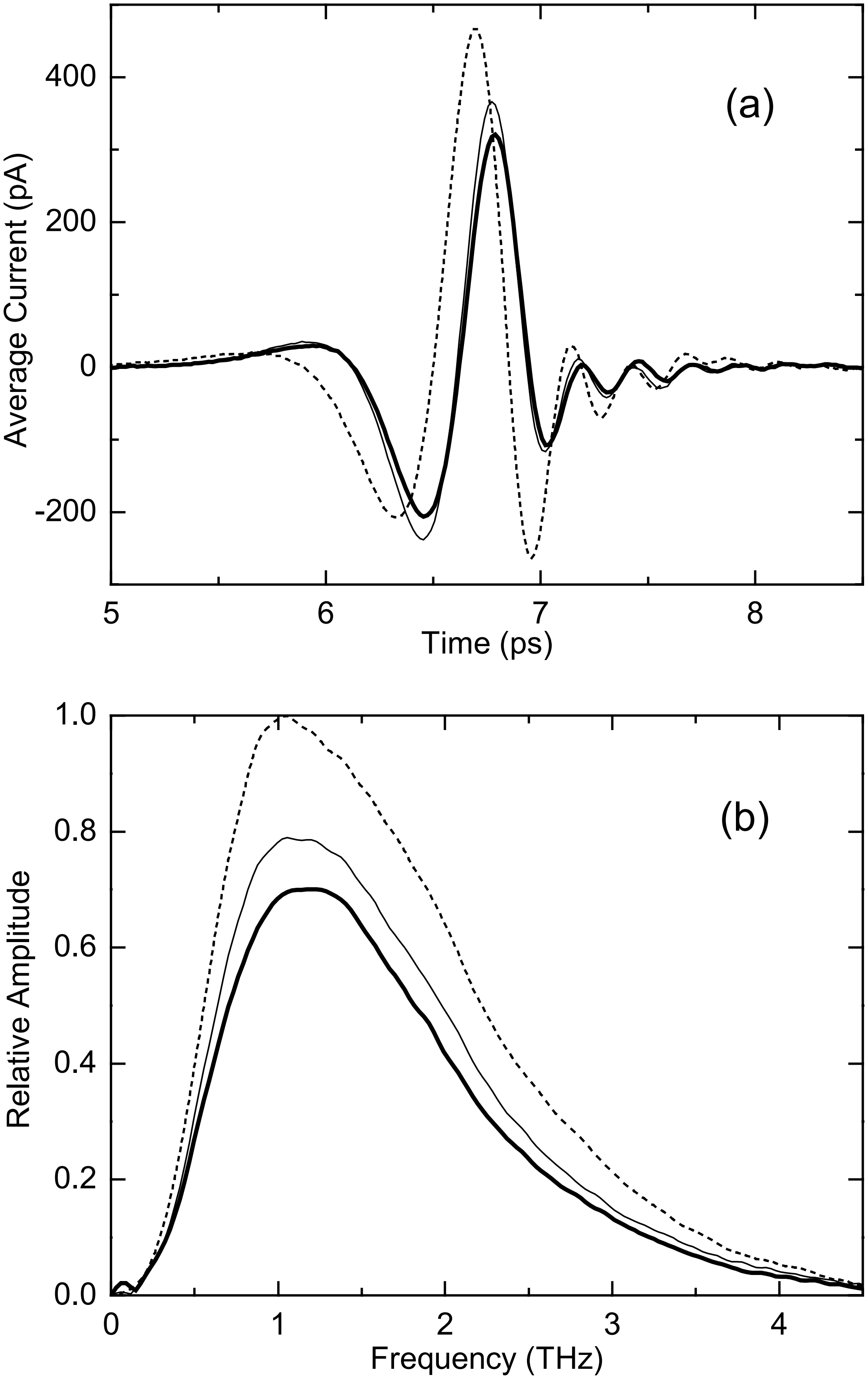

Figure 4-3. Comparison of the reference (dashed line) and propagated pulses (a), and their amplitude spectra (b). The thin and thick solid lines correspond to the output of the short and long waveguides, respectively.

The comparison of the propagated pulses and the reference pulse given in Figure 4-3 (a), plotted to the same time reference, clearly shows almost no dispersive pulse broadening and minimal absorption, unlike any of the previous observations on THz waveguides [1-3,7]. The low-loss nature of the waveguide and the high coupling efficiency is also seen in Figure 4-3 (b), that gives the amplitude spectra of the isolated pulses. This shows a useful input spectrum extending from 0.1 to about 4.5 THz as well. The relative smoothness of the output spectra with no low-frequency cutoff or any oscillations owing to multimode-interference, confirms the single TEM mode behavior of the waveguide [1,2]. The single-mode nature of propagation through the waveguides is actually apparent by the very clean output pulses that closely resemble the input reference pulse. The slight reshaping observed between the two propagated pulses is due to the frequency-dependent absorption and to a small amount of dispersion inherent in any system with a frequency-dependent loss process, introduced by the finite conductivity of copper. The minor change in shape and the slight temporal shift between the reference pulse and the propagated pulses are mainly due to the phase and amplitude changes caused by the frequency dependent nature of the coupling into and out of the guide. The phase was affected as a result of the waveguide (entrance/exit) face moving away from the Gaussian beam waist, and the radius of curvature of the phase-front of the beam coming into play.

It should be noted that the time-domain pulses shown are from single scans, where no averaging has been carried out to improve the signal-to-noise ratio.

Theoretical Analysis

The fundamental equation governing the input and output relationship of the system is identical to Equation (3-1). The phase term in Equation (3-1) illustrates the experimental condition that the spatial distance between the transmitter and receiver is fixed. Within this fixed distance, the cylindrical lenses are moved and the waveguide is inserted as shown in Figure 4-1. This provides an absolute time reference with no temporal effects coming into play due to the movement of the lenses. The only time shifts in Figures 4-2 (a)-(c) are due to the complex coupling coefficient, and the difference between the propagation velocity and free-space velocity *c*.

Modal Analysis

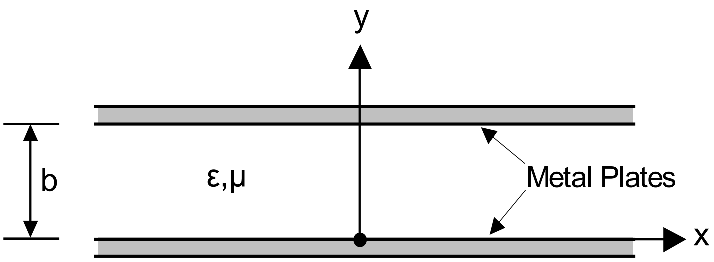

Figure 4-4. Transverse cross-section of the parallel-plate waveguide.

Based on the well-known two-dimensional analysis [24], for an input electric field that is linearly polarized in a direction (y) normal to the plane of the plates, only TM modes can exist in the waveguide. For a loss-less case, with z-directed propagation, the non-vanishing terms of the field components are

$$H_x = A_m \cos\left(\frac{m\pi}{b} y\right) e^{-j\beta_z z} \tag{4-1}$$

$$E_y = -\frac{A_m \beta_z}{\omega_o \varepsilon} \cos\left(\frac{m\pi}{b} y\right) e^{-j\beta_z z} \tag{4-2}$$

$$E_z = \frac{A_m}{j\omega_o \varepsilon} \left(\frac{m\pi}{b}\right) \sin\left(\frac{m\pi}{b} y\right) e^{-j\beta_z z}, \tag{4-3}$$

$$\text{with } \beta_z^2 + \left(\frac{m\pi}{b}\right)^2 = \beta_o^2 = \omega_o^2 \mu \varepsilon, \tag{4-4}$$

where $m = 0, 1, 2, \ldots$ and $0 \le y \le b$. Here, ω, μ, ε, β have their usual meanings, b is the plate separation, A_m is a constant which depends on the excitation of the waveguide, and subscript o stands for free-space quantities.

The cutoff frequencies are given by

$$f_{cm} = \frac{mc}{2bn_d}, \tag{4-5}$$

where n_d is the refractive index of the insulating medium between the plates. The lowest order TM_0 mode, which is in fact a TEM mode, has no cutoff frequency, and for perfectly conducting plates, has no GVD, with both υ_g and υ_p being equal to c, and the wave impedance equal to the intrinsic impedance of free-space η_o, for the air-filled case.

It should be emphasized here, that the TEM mode having *no cutoff* frequency is a subtle difference from the earlier case of the slab waveguide, where the dominant mode has a *zero cutoff* frequency. The TEM mode with no cutoff has the unique ability to propagate (transmit) even a dc signal, whereas the mode with a zero cutoff cannot. This is clear because the parallel-plate waveguide is in fact a two-conductor transmission line, whereas the slab waveguide is just one dielectric slab.

Quasi-optic Coupling

The mode profile, which is expressed in terms of the magnitude of the y-component of the electric field, has a spatial dependence of $\cos[m\pi y/b]$ as given by Equation (4-2), where $y = b/2$ corresponds to the axis of the guide. This dependence, shown in Figure 4-5, results in an even uniform profile for the TEM mode, an odd profile for the TM_1 mode, and an even profile for the TM_2 mode. Therefore, the next higher-order mode following the dominant TEM, that a y-polarized, on-axis, even Gaussian beam will couple onto, is the TM_2 mode. Consequently, single TEM mode propagation is achievable by spacing the plates such that the cutoff frequency of the TM_2 mode falls outside the input spectrum.

It should be noted that here, unlike in the slab waveguide, the mode profiles have no frequency dependence. This is due to the strong boundary conditions at the air-conductor interface.

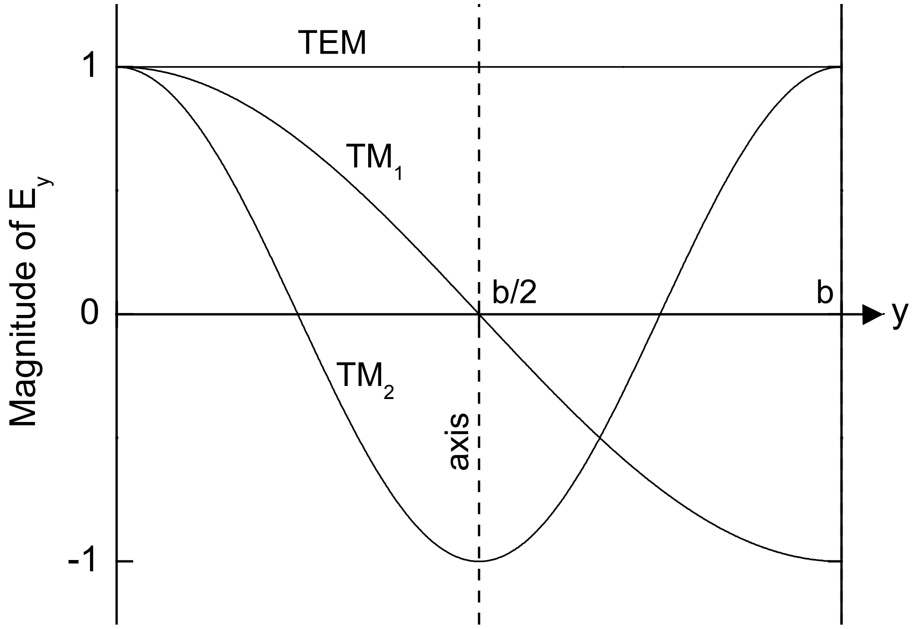

Figure 4-5. Mode profiles of the first three modes.

Propagation Loss

In general, the propagation loss in a parallel-plate waveguide is two-fold; a loss arising from the conduction currents in the metal plates called the *conduction loss*, and a loss arising from the dielectric medium between the plates called the *dielectric loss*. In the case of an air-filled guide, the only loss involved is the conduction loss, which is an obvious advantage, out of the many that are described in this study.

Theoretically, for plates made of a perfectly conducting (infinite conductivity) metal, the conduction loss associated with any given mode would be ideally zero. But in practice, there would be a loss introduced by the finite conductivity of the metal. This conduction loss, which can be expressed in terms of an amplitude absorption constant α, is given by [24]

$$\alpha = \frac{\delta_m R n_d}{\eta_o b \sqrt{1-\left(\lambda_o / \lambda_{cm}\right)^2}}, \qquad (4\text{-}6)$$

where $\begin{array}{l} \delta_m = 1 \;\; if \;\; m = 0, \\ \delta_m = 2 \;\; if \;\; m \neq 0, \end{array}$ and $R = 10.88 \times 10^{-3} \sqrt{\frac{10^7}{\sigma \lambda_o}}$.

The value of the characteristic resistance R will be in ohms, if the conductivity σ is in siemens per meter, and the free-space wavelength λ_o is in meters. The change in the skin-depth with frequency, gives rise to a frequency dependence in the value of α.

Based on the above Equation (4-6), it is clear that the conduction loss increases with increasing n_d (which may seem counter-intuitive, because the conduction loss seemingly depends on the dielectric medium), and decreases with increasing b. Once again, an air-filled guide proves to be beneficial, obviously providing the minimum conduction loss, since the conduction loss increases with increasing n_d. It may also seem possible to reduce the loss without bound, by increasing the plate separation b. But, more and more higher-order modes will come into play with a larger value of b, thereby putting a limit on the separation. Therefore, there is a trade-off in achieving single-mode propagation while optimizing the loss.

In the above discussion regarding the propagation loss, nothing much was mentioned about the dielectric loss, since the present experiment was carried out using air-filled guides. If a dielectric medium other than air had been used, then the dielectric loss for the TEM mode would have been the direct absorption loss of the bulk dielectric material.

Kramers-Kronig Analysis

It was mentioned that for an air-filled guide with perfectly conducting plates, the GVD for the TEM mode is zero. But with a finite conductivity, a frequency-dependent loss process comes into affect, which in turn has to result in some dispersion mechanism. The proof of this argument lies within the Kramers-Kronig relations, which have to be satisfied by any physical system under the conditions of causality and linearity [25]. In general, the attenuation and dispersion of any physical system is inter-related through the Kramers-Kronig relations. If one quantity is known (as a function of frequency), then the other one can be deduced analytically using these relations.

The exact analysis using the Kramers-Kronig integrals requires the full frequency dependence ranging from $\omega = 0$ to $\omega = \infty$. In the present study, the goal was to derive the dispersion associated with the TEM mode, starting from the frequency-dependent loss given by Equation (4-6). It is clear that this loss curve, which has a smooth square-root dependence in the THz frequency range, is not applicable to the complete frequency spectrum ranging from 0 to ∞. Therefore, it was deemed necessary to use the nearly local approximation to the Kramers-Kronig relations [25], which is expressed as

$$\alpha(\omega) = \frac{\pi\omega^2}{2\upsilon_o^2}\frac{d\upsilon(\omega)}{d\omega} \tag{4-7}$$

$$\upsilon(\omega) = \upsilon_o + \frac{2\upsilon_o^2}{\pi}\int_{\omega_o}^{\omega}\frac{\alpha(\omega')}{\omega'^2}\,d\omega', \tag{4-8}$$

where $\alpha(\omega)$ and $\upsilon(\omega)$ are the attenuation constant and phase velocity, respectively, at angular frequency ω, and υ_o is some reference velocity at some reference angular frequency ω_o. It has been demonstrated, that this nearly local approximation represents an accurate description of the relationship between the attenuation and the dispersion of the system, in the absence of rapid variations with frequency [25].

If the phase velocity at a particular reference frequency is known, Equation (4-8) can be used to derive the local variation of the velocity around this value, starting from the frequency-dependent loss, provided that the loss curve is relatively smooth.

For the air-filled guide, Equation (4-8) reduces to

$$\upsilon = \upsilon_o - \frac{4\upsilon_o^2 k}{\pi}\left(\frac{1}{\sqrt{\omega}} - \frac{1}{\sqrt{\omega_o}}\right), \tag{4-9}$$

where $k = \frac{10.88\times10^{-3}}{\eta_o b}\sqrt{\frac{10^7}{2\pi c\sigma}}$.

Comparison of Theory with Experiment

In the present study, the final comparison between theory and experiment was carried out in a somewhat different manner to the earlier case. Here, the theoretical evaluation of the amplitude coupling coefficient C and the total transmission coefficient T were avoided, in order to simplify the analysis. For the two parallel-plate waveguides that differed in length, the input and output conditions were assumed to be identical, since both had the same plate separation of 108 µm. Therefore, the mode coupling and reflection considerations were taken to be the same for both guides, and the product TC^2 in Equation (3-1) was assumed to be identical for both.

The theoretical loss curves, calculated using Equation (4-6), for the first three TM modes in a copper parallel-plate waveguide having a plate separation of 108 µm are plotted in Figure 4-6 (a). As shown by this, even if some residual coupling to the TM_2 mode did exist, the higher absorption compared to that of the dominant TEM mode would more rapidly attenuate the TM_2 mode with propagation.

As mentioned earlier, the theoretical values of υ_p and υ_g can be derived using β_z that is given in Equation (4-4). Figure 4-6 (b) gives the υ_p and υ_g curves (as a ratio with respect to c) for the first three modes, which shows the high GVD of the TM_1 and TM_2 modes compared to that of the TEM mode. This high GVD is a consequence of the cutoff frequencies inherent to the higher-order modes, whereas there is no cutoff for the TEM mode. The velocity curve for the TEM mode comes out to be a precisely straight line, suggesting a strictly frequency-independent value of c, since perfectly conducting metal plates had been assumed in the initial analysis.

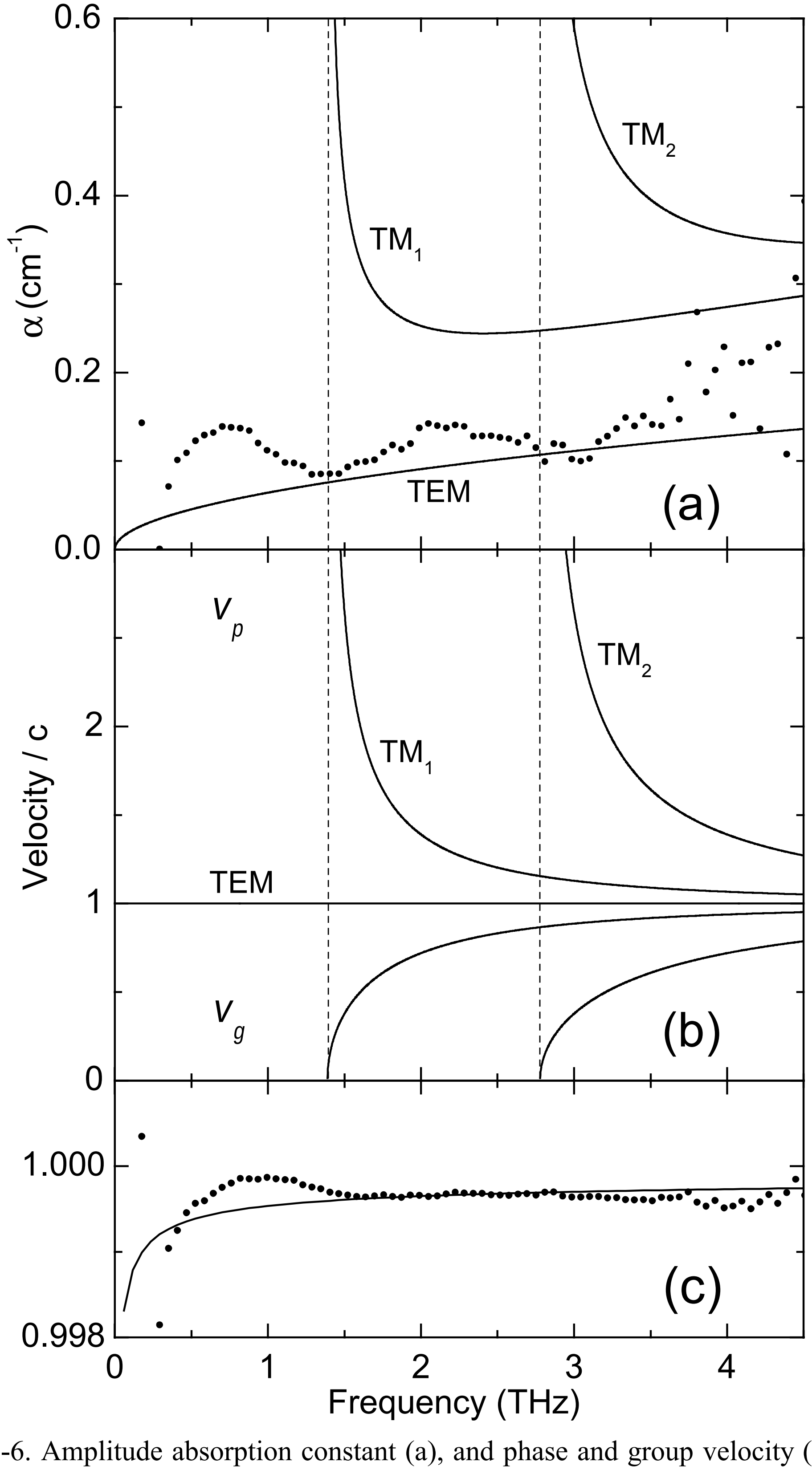

Figure 4-6. Amplitude absorption constant (a), and phase and group velocity (b), for the first three modes. Cutoff conditions are shown by the dashed lines. (c) Blown-up view of (b) in the vicinity of unity. Experimental values are shown by the dots.

The experimental values of α and β_z can be deduced by applying Equation (3-1) to the (Fourier Transformed) data of the short and long waveguides separately, and then taking the complex ratio to eliminate the product TC^2, and then separating the amplitude and phase information. The experimentally determined α is also plotted (dots) in Figure 4-6 (a), and this is consistent with the predicted low absorption for the TEM mode. The discrepancies may be mainly due to the assumption of an identical product TC^2 for both waveguides, when analyzing the data.

In order to compare the experimental value of the velocity dispersion (derived from the experimental value of β_z) with a theoretical value, the nearly local approximation to the Kramers-Kronig relations, was used. Following this analysis, the value of υ_p calculated using Equation (4-9), was compared with the experimental value. Use of the local approximation is justified due to the smooth variation in the loss. This comparison is shown in Figure 4-6 (c), where the theoretical curve (solid line) has been fitted to the experimental values (dots) at 2 THz. The theoretical curve, together with the experimental values, clearly exhibits virtually zero dispersion (with a velocity change of less than 0.1 % within the relevant bandwidth) even under the influence of a finite conductivity. Due to this very slight variation in velocity, if Figure 4-6 (c) had been drawn to the same scale as in Figure 4-6 (b), the curve would still look like a straight line, corresponding to the value of c.

Low Loss TE_1 Mode

In contrast to the TM modes discussed earlier, for an input electric field polarized *parallel* to the metal plates, TE modes will be excited in the parallel-plate waveguide [24]. The cutoff frequencies are given by the same expression as for TM, Equation (4-5), where $m \neq 0$. Therefore, the dominant mode in this case would be the TE_1 mode, having a cutoff frequency of $c/(2bn_d)$.

It is interesting to note that the conduction loss associated with TE modes actually decreases with increasing frequency, away from cutoff, where the conduction loss expressed in terms of an amplitude absorption constant is given by [24]

$$\alpha = \frac{2Rn_d\left(\lambda_o/\lambda_{cm}\right)^2}{\eta_o b\sqrt{1-\left(\lambda_o/\lambda_{cm}\right)^2}}. \tag{4-10}$$

This frequency dependence, illustrated in Figure 4-7, is unlike the case of TM modes, where the loss increases with increasing frequency, away from cutoff. Figure 4-7 shows characteristic loss curves (solid lines) for the TE_1 mode [based on Equation (4-10)], in comparison to those of the TEM mode (dashed lines). Here, the two curves related to each respective mode correspond to plate separations of 100 μm and 200 μm, where air-filled parallel-plate waveguides made of copper have been assumed.

This comparison clearly predicts a much lower loss for the TE_1 mode (away from cutoff) than for the TEM mode. Similar to the TEM mode, the loss can be reduced by increasing the plate separation, which would also increase the probability of producing undesirable multi-mode propagation, for a given input bandwidth. But the mode profile (electric field amplitude) of the TE_1 mode has a $\sin[\pi y/b]$ spatial dependence [24] that is more closely matched to a Gaussian profile than the flat-top profile of the TEM mode.

And this may provide better selectivity of the TE_1 mode, when faced with a possible multi-mode situation, implying the capability of handling a larger plate separation (thereby reducing the loss further) than with the TEM mode.

It should be emphasized that even though the TE_1 mode looks very appealing in terms of propagation loss, it cannot match the performance of the TEM mode in terms of dispersion. Due to the presence of the low frequency cutoff, propagation in the TE_1 mode would result in considerable distortion while being limited in operational bandwidth, compared to TEM mode propagation.

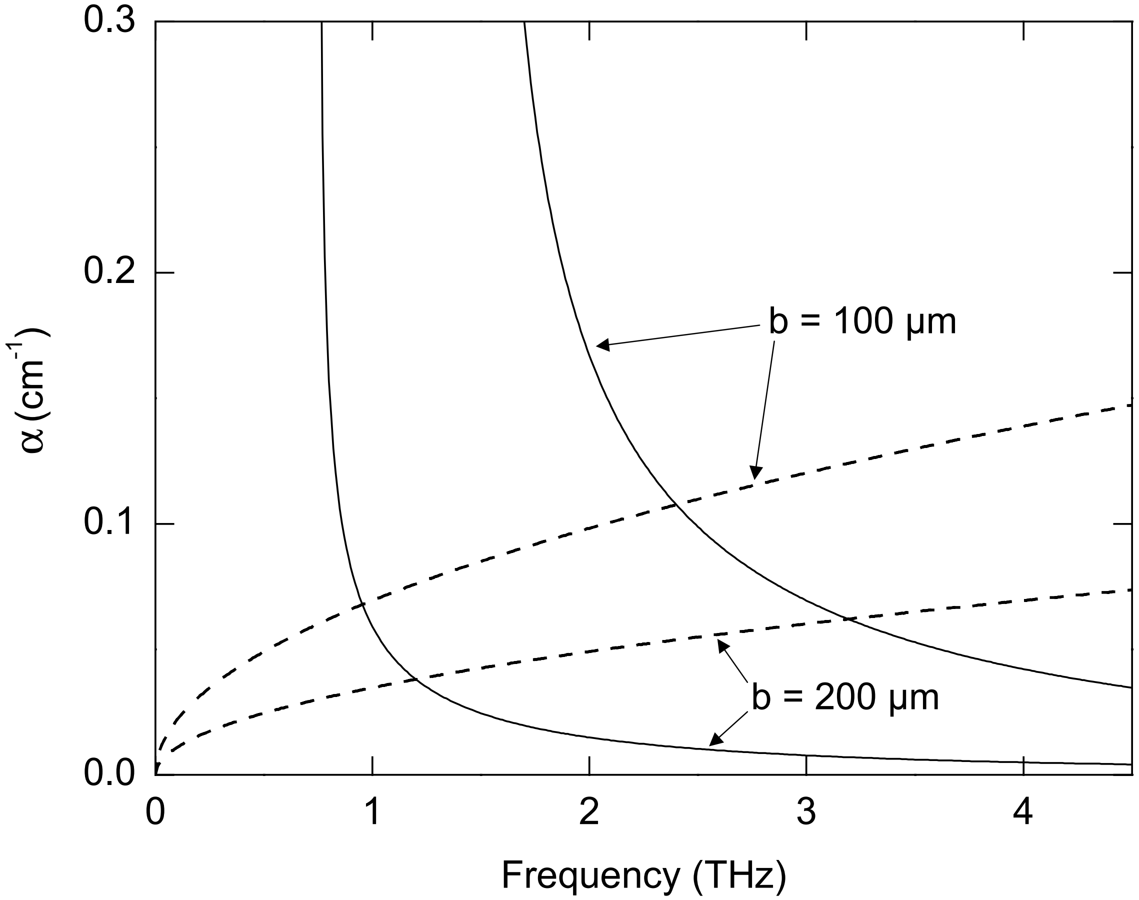

Figure 4-7. Amplitude absorption constant for the TE_1 mode (solid lines), in comparison to that for the TEM mode (dashed lines), for air-filled parallel-plate waveguides made of copper.

CHAPTER V

LONG & FLEXIBLE PARALLEL-PLATE WAVEGUIDE

The goal was to extend the parallel-plate waveguide concept into a physically flexible, practicable, THz interconnect with a substantially long propagation length.

Waveguide Specimens

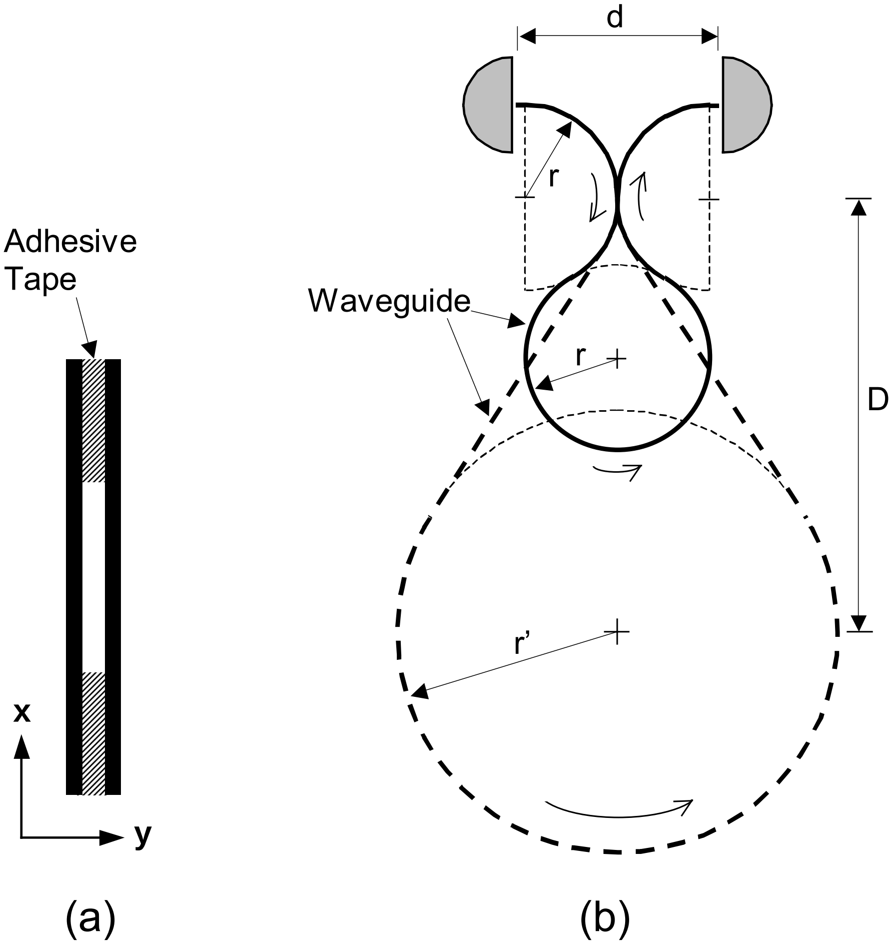

Figure 5-1. (a) Cross-sectional view of the waveguide (not to scale). (b) Plan view of the propagation paths for the 125 mm long (thick solid line), and 250 mm long (thick dashed line) waveguides. The *x*-direction is normal to the plane of paper.

For this experiment, two long parallel-plate waveguides, that were incorporating bends, were fabricated in the laboratory. Each waveguide was constructed using two 100 μm thick copper strips, 35 mm wide and 250 mm (or 125 mm) long. The inner surfaces of the strips were polished using 1500 grit finishing sheets. They were joined together (electrically isolated) lengthwise by double-sided adhesive tape 10 mm wide and 90 μm thick, that provided a flexible air-duct having cross-sectional dimensions of 90 μm × 15 mm between the plates. This is illustrated in Figure 5-1 (a), which shows the cross-section of the waveguide.

Figure 5-1 (b) gives the plan view of the propagation paths for the 125 mm long ($r = 11.5$ mm) and 250 mm long ($r' = 27.5$ mm, $D = 54$ mm) waveguides. The bending of the waveguides (in a plane normal to the plates) facilitated the long propagation paths within the maximum confined space (≈ 24 mm) between the two cylindrical lenses. The *inverted* Ω shape optimized the curvature of the waveguides within this limited space. The cylindrical lenses were identical to the ones used in the previous experiment.

Experimental Results

The reference pulse shown in Figure 5-2 (a) is obtained by moving the cylindrical lenses to their confocal position, with no waveguide in place, as described earlier. The small secondary pulse is due to the reflections from the flat surfaces of the two lenses. Propagated pulses through the 125 mm long and 250 mm long parallel-plate waveguides are shown in Figures 5-2 (b) and (c), respectively. Figure 5-2 (b) is the average of 2

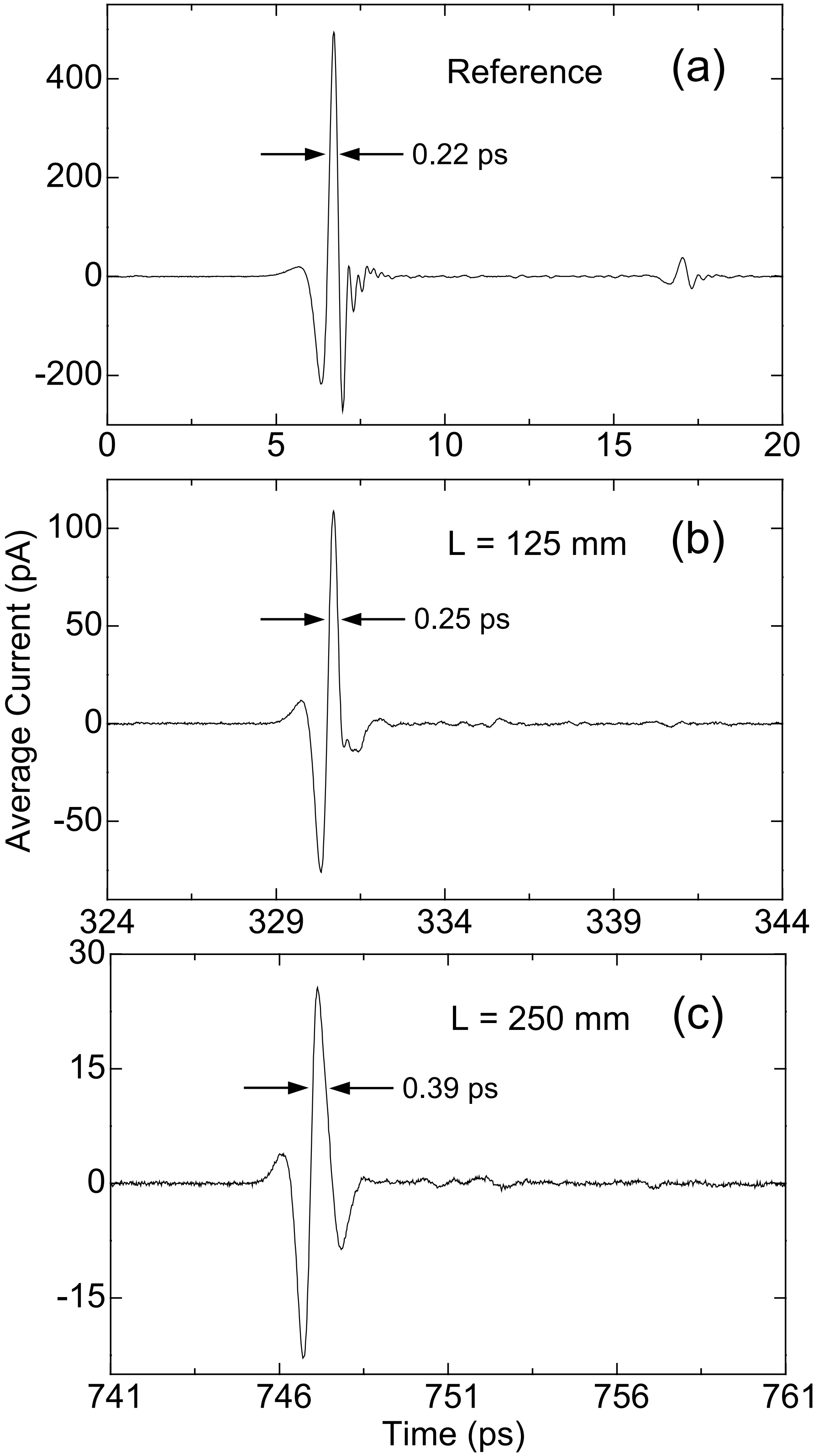

Figure 5-2. Reference pulse (a), the propagated pulse through the 125 mm long waveguide (b), and the propagated pulse through the 250 mm long waveguide (c).

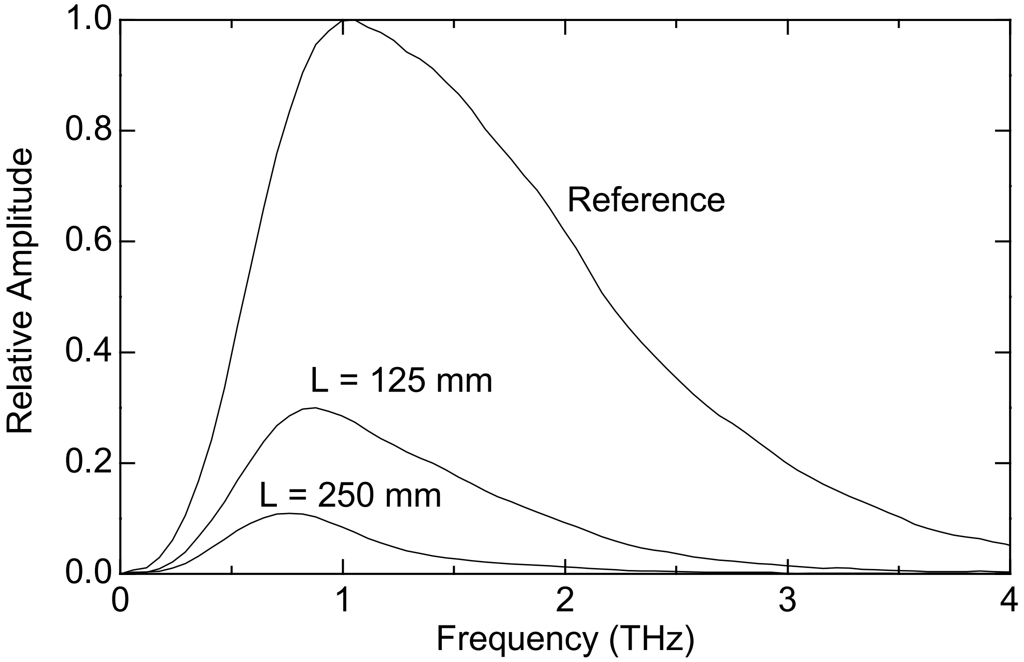

Figure 5-3. Amplitude spectra of the isolated pulses.

scans, and Figure 5-2 (c) is the average of 8 scans. The FWHM is 0.22 ps for the reference pulse, 0.25 ps for the output pulse of the 125 mm long guide, and 0.39 ps for the output pulse of the 250 mm long guide. Characteristic of TEM mode propagation, the propagated pulses clearly exhibit no dispersive pulse broadening. The minimal broadening observed in the output pulses is due to the relative loss in the high frequency content as seen in Figure 5-3, which gives the amplitude spectra of the isolated pulses. The FWHM of the amplitude spectra are 1.62 THz, 1.14 THz, and 0.74 THz, for the reference, the output of the 125 mm long guide, and the output of the 250 mm long guide, respectively. The smoothness of the output spectra revealing no low frequency cutoff, confirms single TEM mode propagation.

Theoretical Analysis

The input and output relationship of the single-mode waveguide system can be written in the frequency domain as

$$E_{out}(\omega) = E_{ref}(\omega) T C_y^2 C_x e^{-j(\beta_z L - \beta_o d)} e^{-\alpha L}, \qquad (5\text{-}1)$$

where $E_{out}(\omega)$, $E_{ref}(\omega)$, T, β_z, β_o, and α are defined as before. C_y is the amplitude coupling coefficient for the y-direction (squared, since assumed to be the same at the input and output), and C_x is the amplitude coupling coefficient for the x-direction (not squared, since unity at the input). L is the distance of propagation, d is the direct free-space path length (along the optic axis) replaced by the guide. It should be noted that the assignment of the x, y, z, rectangular coordinate system, is identical to the previous studies.

The coupling coefficient at the input and output of the waveguide is analyzed using the standard overlap-integral [Equation (3-12)], where the variable separable nature of the respective field quantities is made use of, to breakdown the overall coefficient into the two exclusively one-dimensional parts C_x and C_y. Here, C_y takes into account the similarity of the input Gaussian beam to the guided mode in the y-direction, and C_x takes into account the divergence of the guided mode in the x-direction due to diffraction, assumed to be the same as in free-space. At the input of the waveguide C_x will always be unity, since the guided mode originates at this point. But, at the output C_x will be less than unity, since this effectively gives the overlap between the planar waist profile of a Gaussian beam and the relatively larger spherical profile of the same Gaussian beam at some distance away from the waist position. In the case of a short waveguide this would still be very close to unity, but would drop significantly for a considerably long one, as used in this experiment. Figure 5-4 (a) shows the frequency dependence of C_x calculated separately for the propagation distances of the two guides. Both curves imply that the power transfer drops as the frequency increases, consistent with a relatively high divergence of the beam at high frequencies, as a consequence of propagating away from a

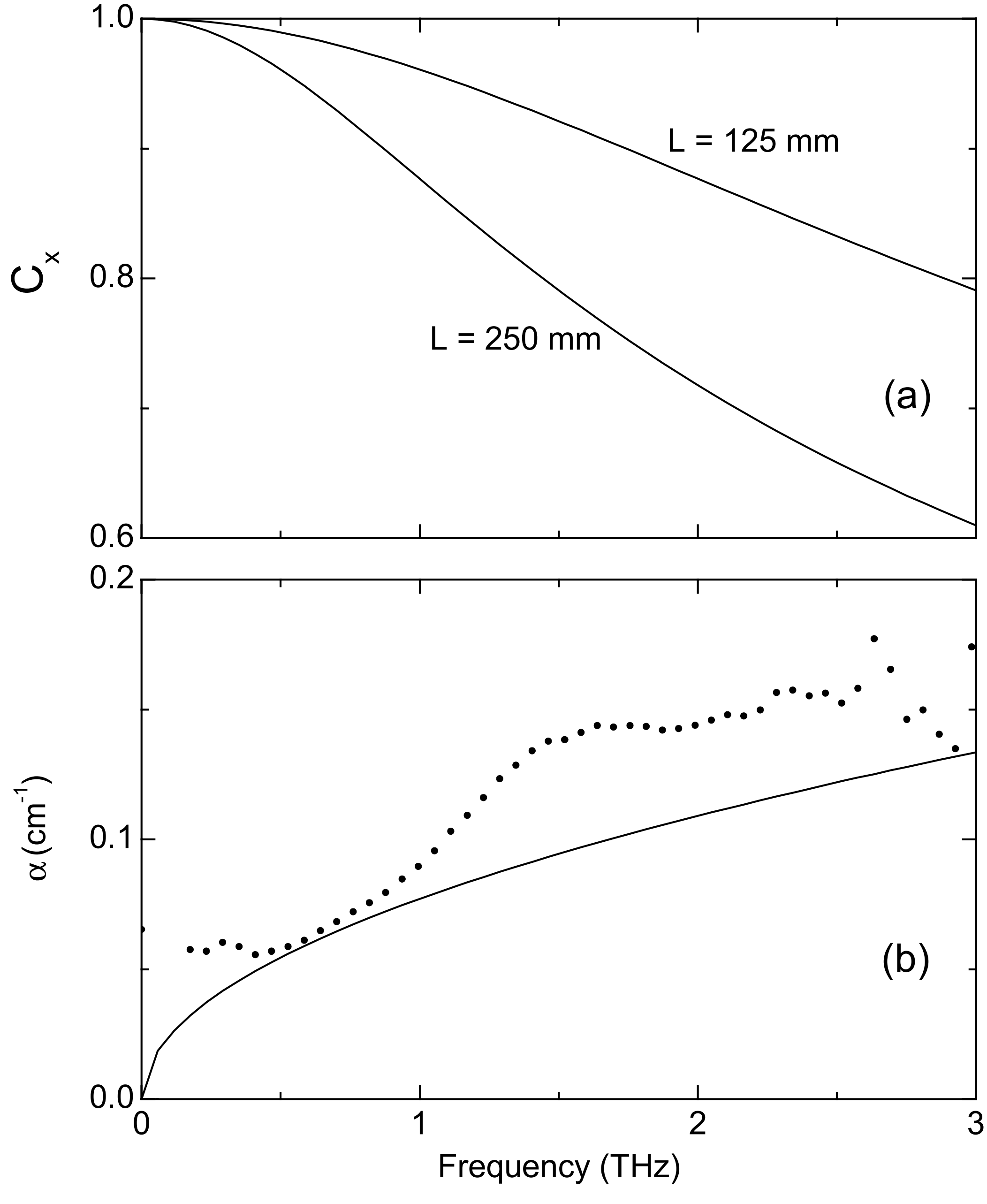

Figure 5-4. (a) One-dimensional amplitude coupling coefficient C_x for the two waveguides. (b) Theoretical (solid line) and experimental values (dots) of the amplitude absorption constant α.

frequency-dependent Gaussian beam waist. And clearly, as shown by the two curves, at a given frequency, the power transfer decreases as the propagation distance increases.

Applying Equation (5-1) to the short and long waveguide data separately and taking the complex ratio, we can eliminate the product TC_y^2, and then after extracting the amplitude information, obtain an expression for the amplitude absorption α as

$$\alpha = \frac{1}{(L_1 - L_2)} \ln \left\| \left[\frac{E_{out2}}{E_{out1}} \right] \left[\frac{C_{x1}}{C_{x2}} \right] \right\|, \tag{5-2}$$

where subscripts 1 and 2 stand for the short and long waveguides, respectively.

Comparison of Theory with Experiment

In order to compare the experimental results with the underlying theory for the TEM mode, the experimental value of α determined using Equation (5-2) was compared with the theoretical value given by Equation (4-6), for an air-filled guide with a plate separation of 90 µm. This comparison shown in Figure 5-4 (b), where the solid line corresponds to the theoretical value, shows consistency between experiment and theory. The observed excess loss can be attributed to undesirable effects due to the bending of the guide, dimensional variations of the waveguide along the transverse and longitudinal directions, and surface roughness and impurities of the copper strips.

A bend, which is a form of discontinuity in the waveguide, can cause undesirable reflections and mode conversions resulting in the loss of power. Even though it may seem somewhat unreasonable to consider any adverse effects due to bending, because of the relatively large radius of curvature (smallest being 11.5 mm) compared to the wavelength, the existence of any (sharp) unevenness in the bent waveguide that may have been caused during the *bending process*, may give rise to undesirable effects [10]. The likelihood of a mode conversion is quite striking, based on the substantial increase in α beyond the frequency of 1.5 THz, which happens to be approximately where the cutoff frequency of the next higher-order TM_1 mode lies. If the TM_1 mode were excited somewhere along the line, it would not be detected at the receiver due to its odd mode profile, resulting in an apparent power loss in the system. And as mentioned in the earlier study, the assumption of identical TC_y^2 terms for the two waveguides, may have also contributed to the overall discrepancy.

CHAPTER VI

GUIDED-WAVE THz-TDS

Single-mode excitation of the dielectric slab waveguide and the parallel-plate metal waveguide opens up the possibility of carrying out novel spectroscopic studies in the far-infrared using guided-waves [26-30]. This THz technology, originally introduced via coplanar transmission lines [31,32], can be termed as Guided-Wave THz-TDS. Out of the many possible spectroscopic applications, this chapter focuses on absorption spectra of thin dielectric films. The film can be in the form of an adsorbed layer (on the surface of the dielectric slab waveguide or on the inner surface of the metal conductors of the parallel-plate waveguide), for example, a single molecular layer (monolayer), or even in the form of a surface reaction such as an oxide layer. In the case of monolayers, due to the polarized nature of the fields, information can also be obtained about molecular orientation (anisotropy) at the surface [29,30].

In this theoretical treatment, the overall analysis is carried out using a perturbational method, where it is assumed that the presence of the thin film only slightly perturbs the fields of the basic waveguide. This allows the use of essentially the same fields (except possibly inside the film itself) and properties of the basic waveguide, when analyzing the waveguide having the film.

The resultant absorption constant for the waveguide having the film can be expressed as the sum of the individual loss constants associated with the basic waveguide and the dielectric film. Therefore, the loss due to the dielectric film can be deduced by taking the difference of the loss constants for the waveguide, with and without the film present. Since the loss due to the thin film would be substantially low (depending on the sensitivity), it is experimentally desirable for the basic waveguide to possess a very low loss. Therefore, high-resistivity silicon would be an ideal choice for the dielectric slab waveguide and copper or silver would be ideal for the parallel-plate waveguide. In the following discussion, theoretical formulae are developed to infer the sensitivity of each waveguide for this type of thin film measurement, first using the dielectric slab waveguide, and then using the parallel-plate waveguide.

Dielectric Slab Waveguide

In the case of the dielectric slab waveguide, there are two approaches for the theoretical development, one is the ray optics approach and the other is the modal field approach. It is appealing to look at the ray optics picture because of its highly intuitive nature, shedding more light into some characteristic propagation aspects of the waveguide.

Ray Optics Approach

When trying to build up the ray optics picture it is meaningful to start by looking at the modal field distribution given in Chapter III. It is clear from Equation (3-2) that the fields within the core region can be represented as a superposition of upward and downward traveling plane waves of the form

$$E_y, E_z, H_x \propto (e^{+j\beta_{yd}y} \pm e^{-j\beta_{yd}y})e^{-j\beta_z z}. \tag{6-1}$$

A possible pictorial representation would be to use a ray that undergoes total internal reflection (TIR) at the top and bottom dielectric-air interfaces, to *symbolize* a bouncing plane wave, as shown in Figure 6-1. The ray can be thought of as a vector normal to the phase-fronts of the plane wave. It should be noted that even though Equation (6-1) seemingly implies two plane waves traveling in different directions, they are in fact the same plane wave, one corresponding to the incident wave and the other to the reflected wave, where the reflection coefficient has a magnitude of unity.

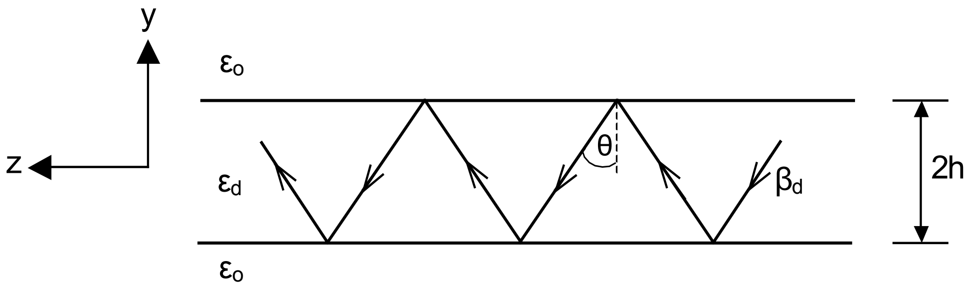

Figure 6-1. Ray path due to total internal reflection.

Based on this ray optics picture,

$$\beta_{yd} = \beta_d \cos\theta \quad \text{and} \quad \beta_z = \beta_d \sin\theta\,, \tag{6-2}$$

where θ is the angle of incidence, and β_d is the phase constant of the plane wave bouncing inside the dielectric slab. The condition for wave-guiding is given as [14,22]

$$4h\beta_d \cos\theta - 2\varphi = 2m\pi\,, \quad m = 0,\ 1,\ 2,\ 3,\ \ldots \tag{6-3}$$

where φ is the phase of the reflection coefficient at the interface.

By using Equation (6-2) and the general relationships in Equation (3-5), it can be shown that for the even values of *m*, Equation (6-3) is mathematically identical to the nonlinear transcendental equation (3-7) obtained via modal analysis for the TM (odd) modes. Accordingly, the odd values of m will correspond to the TM (even) modes. Therefore, results obtained through the ray optics picture would be identical to those obtained via modal analysis.

It can also be shown that for a particular mode of operation, the angle θ decreases as the frequency goes down, and equals the critical angle θ_c at cutoff. Correspondingly, as the frequency goes up, θ gets closer to 90°, where the plane wave approaches grazing incidence.

Internal Reflection Spectroscopy of Thin Films

When analyzing the waveguide with a thin absorbing film on the surface, the ray optics picture simplifies the analysis by allowing the use of well-established concepts in the broad field of Internal Reflection Spectroscopy (IRS) [33]. Since multiple internal reflections are involved, the problem can be closely associated with IRS of thin films. The loss mechanism here is attenuated total reflection (ATR), where part of the energy in the evanescent wave is absorbed by the thin film. The theory is developed, first by deriving the loss for a single reflection using concepts in IRS, and then extending it to include multiple reflections.

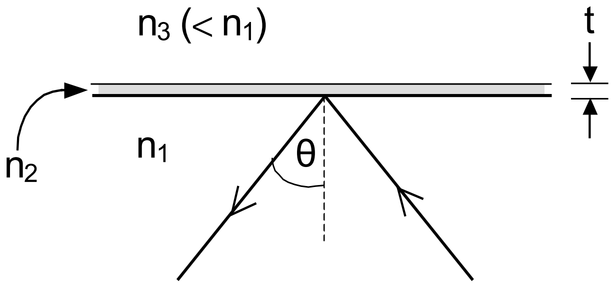

Figure 6-2. Thin film measurement via IRS.

In IRS of thin films, a phenomenological parameter known as the effective thickness t_e is used as a measure of the strength of coupling to the film. This is defined as the thickness of the film material that would give the same absorption for transmission at normal incidence, as that of an internal reflection. The effective thickness for parallel polarization (TM) is [33]

$$t_e = \frac{4n_{21}t\cos\theta\,[(1+n_{32}^4)\sin^2\theta - n_{31}^2]}{(1-n_{31}^2)[(1+n_{31}^2)\sin^2\theta - n_{31}^2]} \tag{6-4}$$

where, $n_{21} = n_2/n_1$, $n_{31} = n_3/n_1$, and $n_{32} = n_3/n_2$.

As shown in Figure 6-2, t is the actual thickness of the film, and n_1, n_2, and n_3, are the refractive indices of the denser medium, film medium, and rarer medium, respectively. With reference to the dielectric slab waveguide, $n_1 = (\varepsilon_d/\varepsilon_o)^{1/2}$ and $n_3 = 1$.

This expression for the effective thickness is an approximation derived under the assumption of a low absorbent, very thin film. Reference [33] states that the accuracy is good to a few percent when $\alpha_f < 0.1\omega n_2/c$ and $t < d_p$, where α_f is the amplitude absorption constant of the film medium, and d_p is the penetration depth of the evanescent field, defined as the distance required for the electric field amplitude to fall to $1/e$ of its value at the surface. From the modal analysis carried out in Chapter III, $d_p = 1/\alpha_{yo}$.

Equation (6-4) shows that the effective thickness is more strongly controlled by media 1 and 3 rather than by media 1 and 2. In fact, it can be shown that measurements can even be made on films having an index $n_2 > n_1$, provided the angle of incidence $\theta > \theta_c$, the critical angle for media 1 and 3, given by $\sin\theta_c = n_{31}$.

Using the concept of effective thickness, the amplitude absorption due to a single internal reflection can be written as $\exp(-\alpha_f t_e)$, and if there are N reflections, then the resultant absorption becomes $\exp(-N\alpha_f t_e)$. For a film coated only on one side of the dielectric slab, N can be calculated by dividing the total length L of the waveguide by the ray spacing required for one reflection.

To properly relate the ray spacing to waveguide geometry, the effect of a phenomenon known as the Goos-Haenchen shift [26,27,34-36] must be incorporated into the ray optics picture. As revealed in Equation (6-3), when the wave undergoes TIR it experiences a phase shift φ that depends on the angle of incidence θ. The effect of this phase shift is to displace the reflected beam parallel to the interface (along z) with respect to the incident beam.

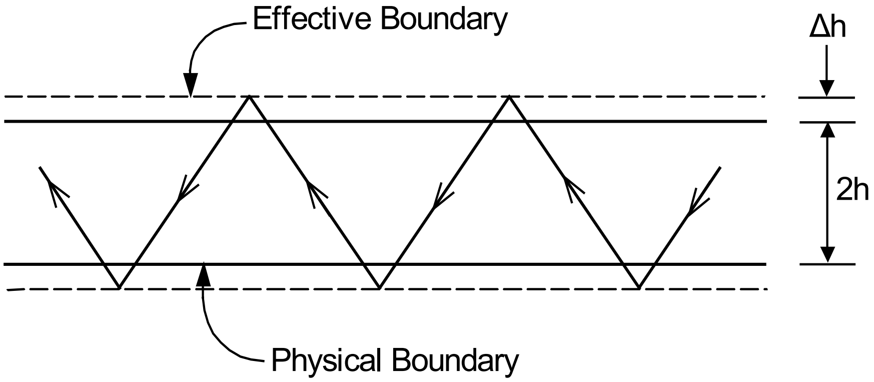

Figure 6-3. Relative locations of the true physical boundary and the effective boundary resulting from Goos-Haenchen shift.

One way of interpreting this lateral shift of the reflected beam would be to consider that the beam is being reflected not from the true physical boundary, but rather from a fictitious boundary located slightly beyond. For TM modes, the distance Δh between the fictitious boundary and the true boundary is given by [34]

$$\Delta h = \left[\frac{\beta_{yd}^2 + \alpha_{yo}^2}{\beta_{yd}^2 + (\varepsilon_d/\varepsilon_o)^2 \alpha_{yo}^2}\right] \frac{\varepsilon_d}{\varepsilon_o \alpha_{yo}}. \tag{6-5}$$

Based on this interpretation, illustrated in Figure 6-3, an effective waveguide thickness can be identified. This is the distance measured between the fictitious boundaries above and below the waveguide core, which is equal to $2(h + \Delta h)$. It should be emphasized that the effect of the Goos-Haenchen shift is negligible for incidence angles much larger than θ_c, but becomes significant when the angle gets closer to θ_c. This behavior can be seen in Equation (6-5), where $\Delta h \rightarrow 0$ when $\theta \rightarrow 90°$ and $\Delta h \rightarrow \infty$ when $\theta \rightarrow \theta_c$, by replacing β_{yd} and α_{yo} with θ using Equations (6-2) and (3-5). Once the value of Δh is known, the total number of reflections can be derived from

$$N = \frac{L}{4(h + \Delta h)} \cot\theta \, . \tag{6-6}$$

Finally, the sensitivity of the waveguide S_{wg} for the thin film measurement can be derived, in comparison to a single-pass transmission measurement at normal incidence, by considering the ratio

$$S_{wg} = \frac{N \, \alpha_f \, t_e}{\alpha_f \, t} = \frac{N \, t_e}{t} \, . \tag{6-7}$$

In order to get a feel for the numbers involved, characteristic plots associated with a typical measurement example are given in Figures 6-4 to 6-6. In this example, a high-resistivity silicon ($n_1 = 3.418$) waveguide, 2 cm long and 50 μm thick, is used to measure the absorption of a film having an index $n_2 = 1.5$. Figure 6-4 (a) shows the variation of the incidence angle θ with frequency, for the dominant TM_0 mode. As stated earlier, at the cutoff frequency of zero, $\theta = \theta_c$, and it increases from this value and gets closer to 90° as the frequency goes up. Figure 6-4 (b) shows the variation of Δh with frequency, where the two curves correspond to two different (vertical) scales. This clearly shows its

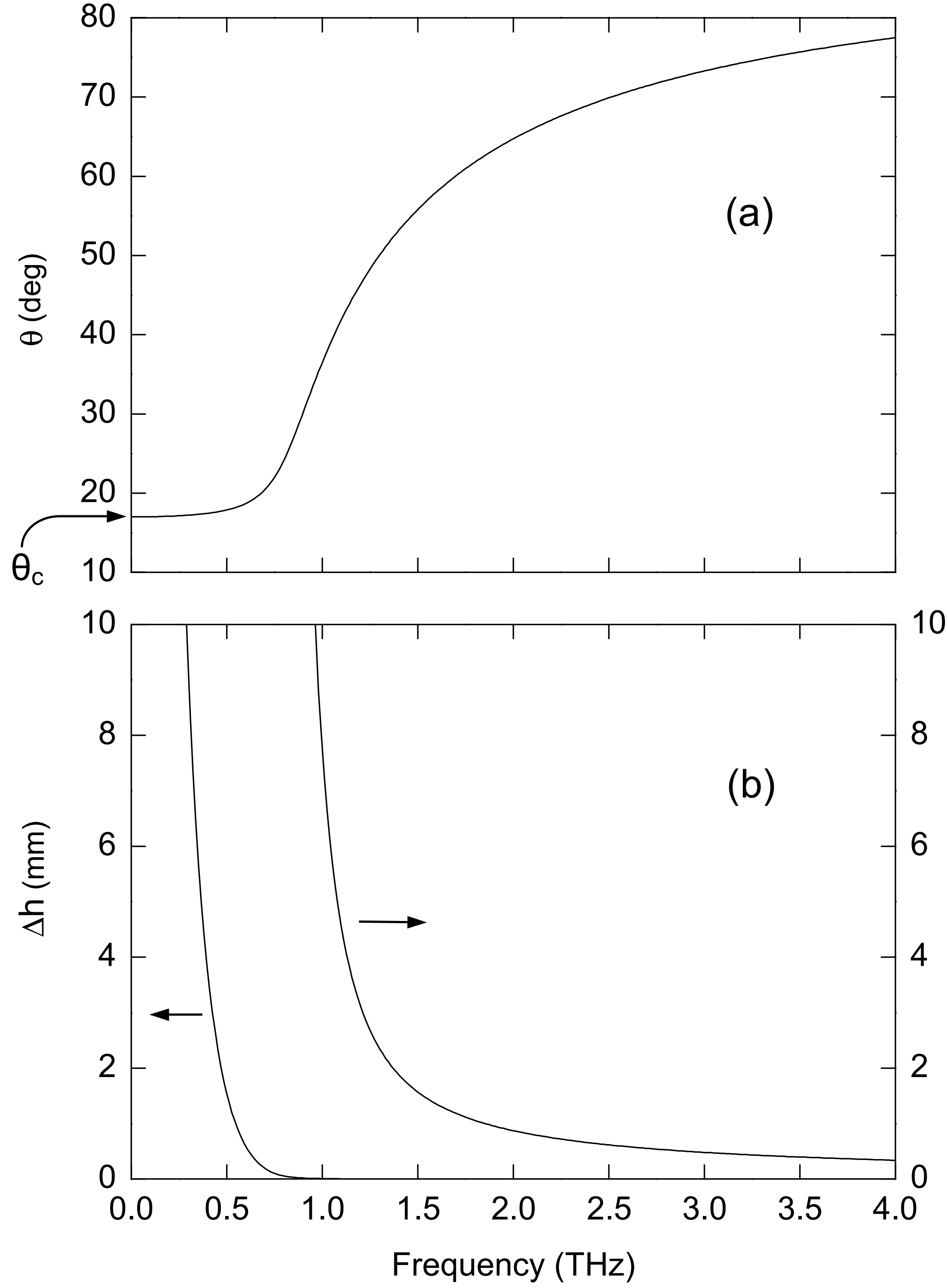

Figure 6-4. (a) Variation of θ with frequency for the TM_0 mode. (b) Variation of Δh with frequency, plotted to two different vertical scales. The curve on the left corresponds to mm, and the curve on the right corresponds to μm.

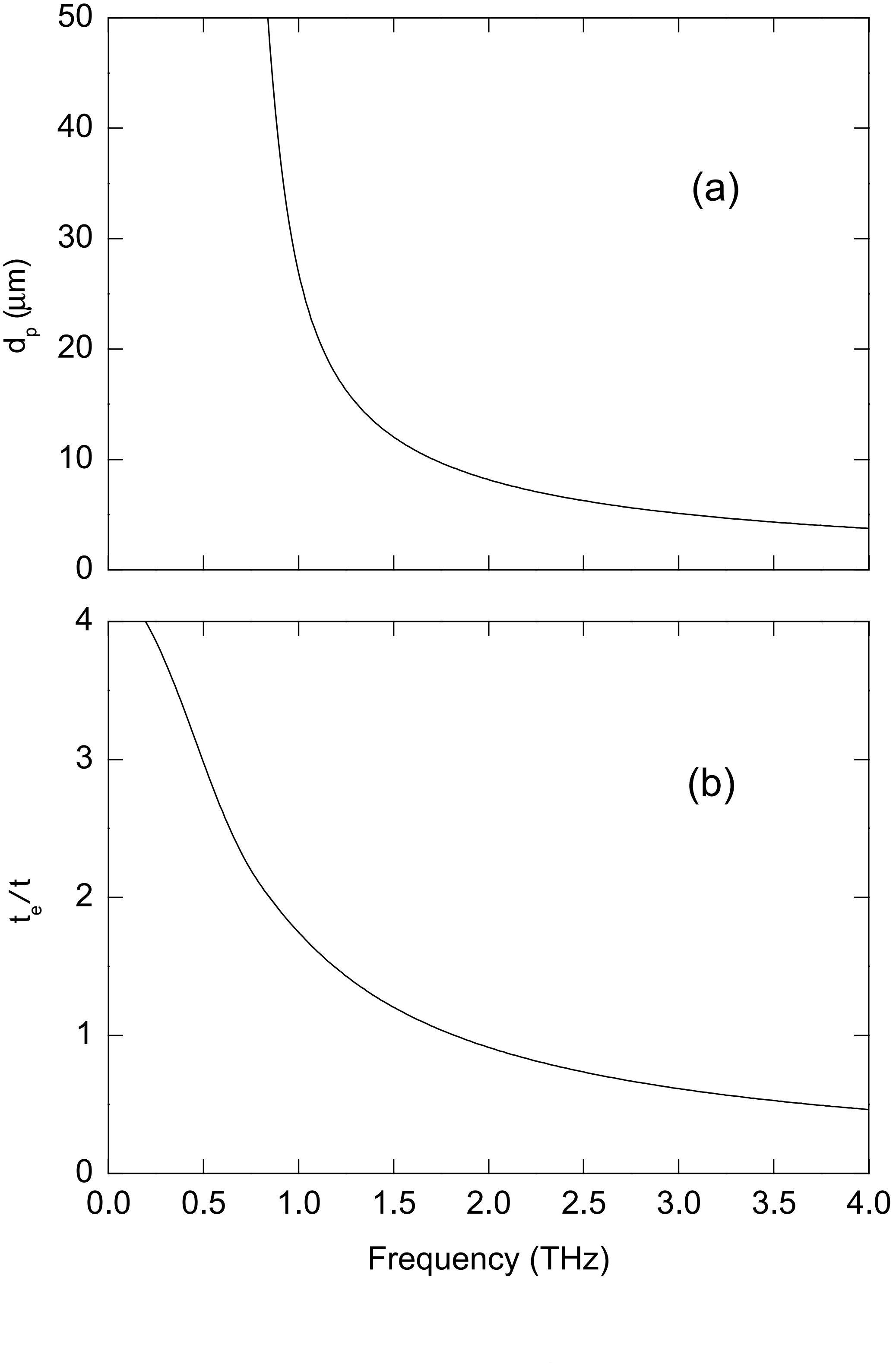

Figure 6-5. Variation of d_p (a), and t_e/t (b), with frequency.

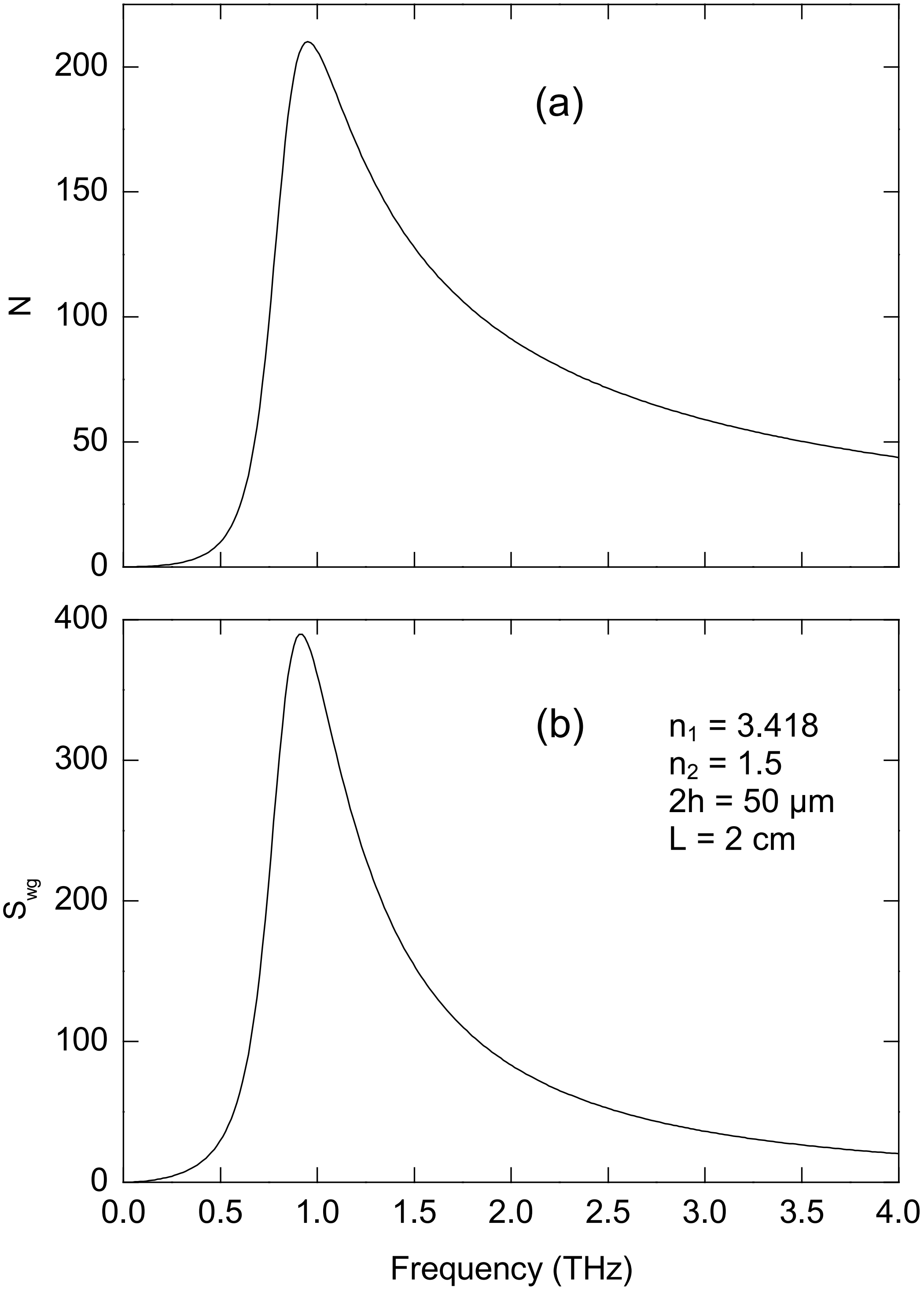

Figure 6-6. Variation of N (a), and S_{wg} (b), with frequency.

significance at the low frequency end, where it blows up near zero. Figure 6-5 (a) shows the change in penetration depth d_p with frequency, which can be used as a guideline when deciding on the actual thickness of the film to be used in the measurement. Figure 6-5 (b) shows the ratio t_e/t as a function of frequency, clearly indicating an advantage towards the low frequency side of the spectrum. Figure 6-6 (a) shows the variation in N, where it is seen to have a maximum near 1 THz. The fact that N decreases drastically towards the low frequency end (instead of continuously rising as the frequency goes down) is a consequence of the Goos-Haenchen shift. Figure 6-6 (b) shows the variation of the sensitivity S_{wg} with frequency, where the curve peaks to about 400 around 0.9 THz, implying the possibility of measuring absorption of samples two orders of magnitude less absorbent, than is possible with a single-pass transmission. The curve also predicts a usable frequency band within which the sensitivity enhancement is attainable.

Modal Field Approach

In this approach, the absorption associated with the thin dielectric film is derived in a more straightforward manner than in the ray optics one, explicitly using the modal fields. This analysis is also governed by the primary assumption that the thin film absorber only slightly perturbs the fields of the basic waveguide.

The derivation is based on Equations (3-8) and (3-9) that were used to calculate the absorption constant for the dielectric slab waveguide. It is understood from Reference [15] that these equations are very general and can be used for any wave-guiding structure consisting of many dielectric layers, provided it has an axially uniform cross-section. Under this condition, Equation (3-8) can be generalized for the case when several layers of the wave-guiding structure have small intrinsic losses. Then, the overall loss will be a weighted average of the form

$$\alpha_T = \sum_i \alpha_i \sqrt{\varepsilon_{r\,i}}\, R'_i \tag{6-8}$$

where α_i and ε_{ri} are respectively, the absorption constant and relative permittivity of the dielectric material in region i, and R'_i is as given in Equation (3-9) where the integral in the numerator is evaluated over the cross-sectional area of region i.

In general, to calculate R'_i associated with a particular dielectric region, the values of the field components inside and also outside the region, are required. In the case of the dielectric slab waveguide with the top surface (in reference to Figure 6-1) coated with a thin film, the fields outside the film region can be assumed to be the same as those for the basic waveguide. Therefore, it is only a matter of finding the electric field inside the film; and of the two possible components E_y and E_z for the TM$_0$ mode, the value of E_z can be taken to be the same as that for the basic waveguide, since this component is tangential to the boundary. The value of the normal component E_y is obtained by matching the electric displacement vector at the film-air interface.

The analysis can be simplified by assuming that the fields are constant over the film thickness. This assumption, also used in IRS of thin films [33], is valid when the film is much thinner than a penetration depth. Therefore, in reference to the modal analysis carried out in Chapter III, the electric field components can be expressed as

$$\left(E_z\right)_{Film} = \left(E_z\right)_{Air} \quad \text{and} \quad \left(E_y\right)_{Film} = \frac{1}{\varepsilon_{r\,f}}\left(E_y\right)_{Air} \tag{6-9}$$

both evaluated at $y = h$. The relative permittivity of the film medium $\varepsilon_{r\,f} = n_2^2$, where n_2 is the refractive index, as used in the ray optics approach.

Using Equation (6-9) in conjunction with the modal field expressions given in Equations (3-2) to (3-4), the value of R'_f (subscript $i \equiv f$ to denote film region) associated with the thin film is evaluated from Equation (3-9), which yields

$$R'_f = \frac{ct\left(\frac{\beta_z^2}{n_2^4} + \alpha_{yo}^2\right)\cos^2(\beta_{yd}h)}{\omega\beta_z\left[\frac{1}{\alpha_{yo}}\cos^2(\beta_{yd}h) + \frac{1}{2n_1^2}\left\{2h + \frac{\sin(2\beta_{yd}h)}{\beta_{yd}}\right\}\right]}. \tag{6-10}$$

Finally, the sensitivity of the waveguide S_{wg} for the thin film measurement can be derived, in comparison to a single-pass transmission measurement as before, by the ratio

$$S_{wg} = \frac{\alpha_f\sqrt{\varepsilon_{rf}}\;R'_f\,L}{\alpha_f\;t} = \frac{n_2\;R'_f\,L}{t}. \tag{6-11}$$

It can be proven (proof given in the appendix) that this expression for S_{wg} is mathematically identical to the one given in Equation (6-7), derived using the ray optics approach. This equality is also illustrated in Figure 6-7, which plots the sensitivity S_{wg} as a function of frequency, using Equation (6-11). The two curves correspond to different film indices ($n_2 = 1.5$ and 3), where the basic waveguide specifications are the same as used in the measurement example ($L = 2$ cm, $2h = 50$ μm, and $n_1 = 3.418$) under the ray optics approach. The lower curve corresponding to $n_2 = 1.5$ is identical to that shown in Figure 6-6 (b). The upper curve corresponding to $n_2 = 3$ (along with the lower curve) predicts how the sensitivity varies with the film index. It is seen that beyond a certain low frequency (about 0.7 THz in this example), well within the enhancement bandwidth of the system, the sensitivity increases as the index goes up.

It should be noted that even though the modal field approach is conceptually different from the ray optics approach, the fact that both methods provide *identical* results, not only strengthens the validity of each methodology as a whole, but also demonstrates the reliability of the particular expressions used to account for phenomena such as the Goos-Haenchen shift.

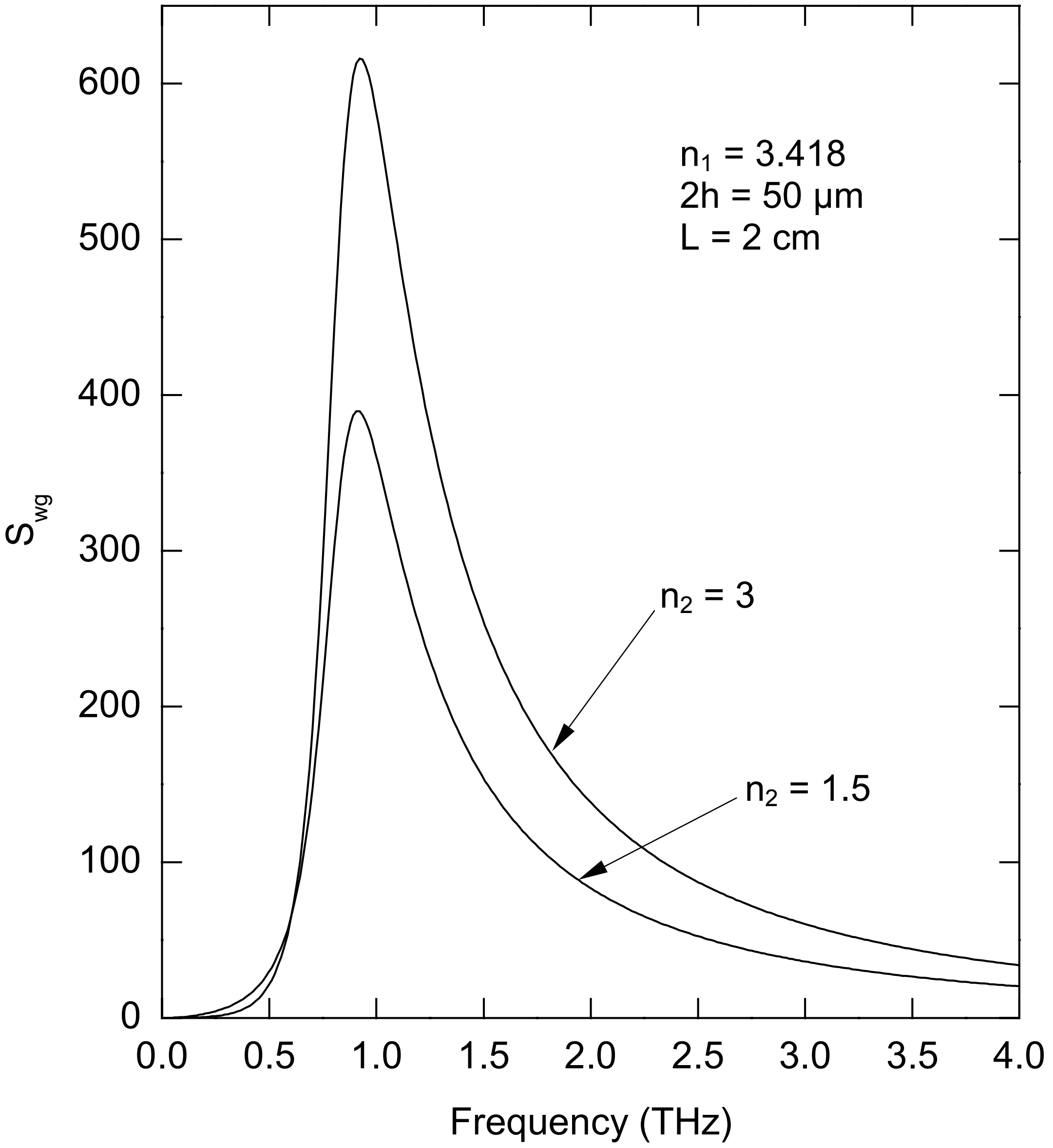

Figure 6-7. Variation of the waveguide sensitivity S_{wg} with frequency, for two different film indices. Upper curve corresponds to an index $n_2 = 3$, and the lower curve corresponds to $n_2 = 1.5$. The lower curve is identical to the one derived using the ray optics approach.

Parallel-Plate Waveguide

In the case of the parallel-plate metal waveguide the modal field approach is used for the theoretical development, under the usual primary assumption of small perturbation due to the thin film absorber. Therefore, similar to the previous derivation, the analysis is carried out starting from the field expressions of the basic waveguide. The fields for the dominant TEM mode are as stated in the modal analysis of Chapter IV, and consists of only the E_y and H_x components, simplifying the analysis considerably.

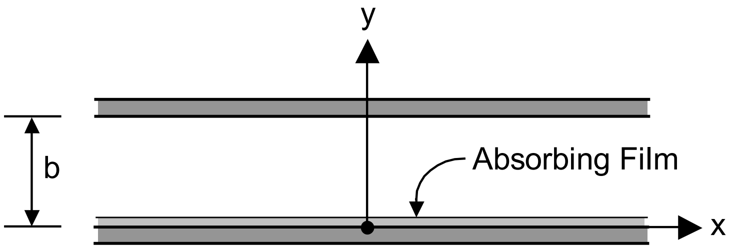

Figure 6-8. Air-filled parallel-plate waveguide with the dielectric film coated on the inner surface of the bottom conductor.

As shown in Figure 6-8, the measurement system consists of an air-filled parallel-plate metal (preferably copper) waveguide with the dielectric film, whose absorption is to be measured, coated on the inner surface of the bottom conductor.

Similar to the modal field approach for the dielectric slab waveguide, the value of the E_y component inside the film is obtained as in Equation (6-9), and the absorption associated with the film is derived using Equations (3-8) and (3-9). And finally, the sensitivity of the waveguide S_{wg} for the thin film measurement, in comparison to a single-pass transmission measurement, can be evaluated to be

$$S_{wg} = \frac{L}{n_2^3\, b} \tag{6-12}$$

where, L is the propagation length of the waveguide, b is the plate separation, and n_2 is the refractive index of the film medium, as used before. It is interesting to note that the same result has been derived (using a stored-energy argument) in Reference [2], for a similar thin film measurement using a hollow rectangular metal waveguide under dominant mode propagation, for frequencies considerably away from cutoff.

As seen from Equation (6-12), due to the uniform nature of the fields, S_{wg} has no frequency dependence. In contrast to the dielectric slab waveguide, the sensitivity decreases as the film index goes up, with a much stronger dependence.

With regards to the measurement example considered for the dielectric slab waveguide, a 2 cm long parallel-plate waveguide with a plate separation of 100 μm will have a sensitivity of approximately 59, when the film index $n_2 = 1.5$. The sensitivity will drop to approximately 7.4 when n_2 increases to 3. To make this waveguide dimensionally more compatible with the dielectric slab waveguide considered earlier, a plate separation of 50 μm can be used. This will increase the sensitivity by a factor of 2, but would also increase the absorption of the basic waveguide by the same factor, and may not result in an overall gain.

CHAPTER VII

CONCLUSIONS

In this dissertation, two planar waveguides, the dielectric slab waveguide and the parallel-plate metal waveguide, were investigated via the propagation of input subps pulses, for the use of technical and fundamental research applications in the far-infrared frequency range. All of the experimentally observed features were explained in detail using classical waveguide theory and quasi-optical theory. The crux of the data analysis was carried out in the frequency-domain, by transforming the time-domain data into the frequency-domain using the Discrete Fourier Transform.

The first part of the study demonstrated the feasibility of the dielectric slab waveguide as a low-loss, single-mode transmission line that can be used for the THz region, capable of utilizing efficient quasi-optic coupling techniques. The substantial GVD dictates only frequency-domain applications to be more promising, hindering the possibility of undistorted subps pulse propagation. Ultra low-loss lines are possible by reducing the thickness of the slab such that most of the guided energy propagates outside the core region. The performance could be further enhanced by using a very low-loss dielectric material such as high-resistivity silicon, that has a power absorption constant in the order of 0.05 cm^{-1} at THz frequencies. Since the GVD can have a sign opposite to that of metal-tube and fiber waveguides, mutual pulse compression should be possible, in analogy to dispersion compensation in optical fibers. Backed by the ability of achieving low-loss single-mode propagation, the dielectric slab waveguide is particularly well adapted for Guided-Wave THz-TDS of surface-specific molecular adsorption layers, or other thin films coating the waveguides, due to the extensive fringing fields of the propagating THz waves. Though it has not been mentioned in the study, due to the one-dimensional nature of the guide, there may be additional losses caused by the divergence of the beam in the unguided dimension, depending on the propagation length, and also on the refractive index of the dielectric material forming the slab.

The second part of the study demonstrated the excellent performance of the parallel-plate metal waveguide as a wideband THz interconnect that is ideal for undistorted subps pulse propagation. It was shown, for an air-filled parallel-plate waveguide made of copper, that in addition to the GVD being virtually nil, it also has a very low propagation loss, as well as very good quasi-optic coupling properties with very low reflection losses. It was also pointed out that the propagation loss could be reduced further by using the TE_1 mode instead of the TEM mode, but while suffering from dispersion.

As mentioned for the dielectric slab waveguide, the metal plates could be coated with films of other metals and alloys, Langmuir-Blodgett films, or conducting polymers. These materials could then be characterized in the frequency-domain by Guided-Wave THz-TDS. The undistorted propagation of subps pulses opens the door to many new time-domain studies as well, that are not possible with any of the earlier THz waveguides including the dielectric slab waveguide. A unique application for high-power TEM THz pulses would be the study of nonlinear pulse propagation, demonstrating nonlinear coherent effects of samples filling the space between the metal plates. For what is believed to be the first time, it was shown that a THz pulse propagating in a waveguide can maintain its spatial focus for arbitrarily long paths without temporal broadening, thereby enormously increasing the effects of nonlinear interactions. This situation is similar to the nonlinear enhancement obtained with optical fibers. Similar to the dielectric slab waveguide, the only drawback of the parallel-plate wavguide is the one-dimensional nature of the guiding structure. Depending on the length of the guide, additional losses can come into play due to the divergence of the beam in the unguided dimension.

The third part of the study, that extended the concept of the parallel-plate waveguide into a long and flexible interconnect, demonstrated better performance than any other THz interconnect to date. This physically flexible metal ribbon waveguide, having low loss and negligible GVD, transmitted a subps THz pulse a quarter of a meter in distance, with an excellent output signal-to-noise ratio. This demonstration shows that chip-to-chip THz guided-wave interconnections with data rates approaching Tb/s are feasible. In reference to the particular composition of the guiding structure used in this experiment, as the beam spreads in the unguided dimension (x), it may be incident upon the adhesive tape (used primarily to provide the spacing for the metal plates) boundary. To avoid any significant effects (due to reflections) from this boundary, this tape would have to be either transparent or a good absorber. No such effects were observed in the experiment.

The last part of the study, being purely theoretical, concentrated on deriving the absorption spectra of very thin dielectric films using the dielectric slab waveguide and the parallel-plate metal waveguide as measuring tools, highlighting the importance of Guided-Wave THz-TDS. In developing the theoretical formulae for the dielectric slab waveguide, two different approaches were used, one involving the modal fields and the other involving a ray optics picture. It was shown that both methods converged to give identical results, strengthening the validity of the derivation. This derivation predicted that the dielectric slab waveguide could be used to measure absorption of samples two orders of magnitude less absorbent, than is possible with a single-pass transmission measurement; a highly sensitive *evanescent field sensor*. Even though the parallel-plate metal waveguide (with comparable dimensions) was found to be less attractive than the dielectric slab waveguide in terms of sensitivity, it has the potential of being useful in measurement situations where the dielectric slab waveguide is not practicable.

CHAPTER VIII

REFERENCES

1. R. W. McGowan, G. Gallot, and D. Grischkowsky, "Propagation of Ultrawideband Short Pulses of Terahertz Radiation through Submillimeter-Diameter Circular Waveguides", Optics Letts., Vol. 24, No. 20, 1431-1433 (1999).
2. G. Gallot, S. P. Jamison, R. W. McGowan, and D. Grischkowsky, "Terahertz Waveguides", J. Opt. Soc. Am. B, Vol. 17, No. 5, 851-863 (2000).
3. S. P. Jamison, R. W. McGowan, and D. Grischkowsky, "Single-Mode Waveguide Propagation and Reshaping of Sub-Ps Terahertz Pulses in Sapphire Fibers", Appl. Phys. Lett., Vol. 76, No. 15, 1987-1989 (2000).
4. D. Grischkowsky, "Optoelectronic Characterization of Transmission Lines and Waveguides by Terahertz Time-Domain Spectroscopy", IEEE J. Sel. Top. Quant. Electron., Vol. 6, No. 6, 1122-1135 (2000).
5. C. Yeh, F. I. Shimabukuro, and J. Chu, "Ultralow Loss Dielectric Ribbon Waveguide for Millimeter/Submillimeter Waves", Appl. Phys. Lett., Vol. 54, No. 12, 1183-1185 (1989).
6. J. E. Goell and R. D. Standley, "Integrated Optical Circuits", Proc. IEEE, Vol. 58, No. 10, 1504-1512 (1970).
7. R. Mendis and D. Grischkowsky, "Plastic Ribbon THz Waveguides", J. Appl. Phys., Vol. 88, No. 7, 4449-4451 (2000).
8. R. Mendis and D. Grischkowsky, "Undistorted Guided-Wave Propagation of Subpicosecond Terahertz Pulses", Optics Letts., Vol. 26, No. 11, 846-848 (2001).

9. R. Mendis and D. Grischkowsky, “THz Interconnect with Low Loss and Low Group Velocity Dispersion”, IEEE Microwave Wireless Comp. Lett., to be published.
10. E. Garmire, T. McMahon, and M. Bass, “Flexible Infrared Waveguides for High-Power Transmission”, IEEE J. Quant. Electron., Vol. 16, No. 1, 23-32 (1980).
11. M. van Exter and D. Grischkowsky, “Characterization of an Optoelectronic Terahertz Beam System”, IEEE Trans. Microwave Theory Tech., Vol. 38, No. 11, 1684-1691 (1990).
12. D. Grischkowsky, S. Keiding, M. van Exter, and Ch. Fattinger, “Far-Infrared Time-Domain Spectroscopy with Terahertz Beams of Dielectrics and Semiconductors”, J. Opt. Soc. Am. B, Vol. 7, No. 10, 2006-2015 (1990).
13. J. Lesurf, “Millimeter-Wave Optics, Devices and Systems”, Adam Hilger, Bristol and New York (1990), p. 14.
14. C. A. Balanis, “Advanced Engineering Electromagnetics”, Wiley, New York (1989), pp. 414-441.
15. W. M. Elsasser, “Attenuation in a Dielectric Circular Rod”, J. Appl. Phys., Vol. 20, 1193-1196 (1949).
16. D. Marcuse, “Light Transmission Optics”, Van Nostrand Reinhold, New York (1972), pp. 305-326.
17. J. R. Birch, J. D. Dromey, and J. Lesurf, “The Optical Constants of some Common Low-Loss Polymers between 4 and 40 cm^{-1}”, Infrared Phys., Vol. 21, 225-228 (1981).
18. J. R. Birch, “The Far Infrared Optical Constants of Polyethylene”, Infrared Phys., Vol. 30, No. 2, 195-197 (1990).

19. R. F. Harrington, "Time-Harmonic Electromagnetic Fields", McGraw-Hill, New York (1961), pp. 171-173.
20. M. Bouda, Y. Nakano, and K. Tada, "Wide-Angle Coupling to Multi-Mode Interference Devices – A Novel Concept for Compacting Photonic Integrated Circuits", IEICE Trans. Electron., Vol. E80-C, No. 5, 640-645 (1997).
21. J. W. Mink and F. K. Schwering, "A Hybrid Dielectric Slab-Beam Waveguide for the Sub-Millimeter Wave Region", IEEE Trans. Microwave Theory Tech., Vol. 41, No. 10, 1720-1729 (1993).
22. P. K. Tien, "Light Waves in Thin Films and Integrated Optics", Appl. Optics, Vol. 10, No. 11, 2395-2413 (1971).
23. G. W. Chantry, J. W. Fleming, P. M. Smith, M. Cudby, and H. A. Willis, "Far Infrared and Millimeter-Wave Absorption Spectra of some Low-Loss Polymers", Chem. Phys. Lett., Vol. 10, No. 4, 473-477 (1971).
24. N. Marcuvitz, "Waveguide Handbook", Peter Peregrinus, London (1993), Chap. 2.
25. M. O'Donnell, E. T. Jaynes, and J. G. Miller, "Kramers-Kronig Relationship between Ultrasonic Attenuation and Phase Velocity", J. Acoust. Soc. Am., Vol. 69, No. 3, 696-701 (1981).
26. T. E. Plowman, S. S. Saavedra, and W. M. Reichert, "Planar Integrated Optical Methods for Examining Thin Films and their Surface Adlayers", Biomaterials, Vol. 19, 341-355 (1998).
27. L. Kang and R. E. Dessy, "Slab Waveguides in Chemistry", CRC Crit. Rev. Anal. Chem., Vol. 21, No. 6, 377-388 (1990).
28. G. Stewart and B. Culshaw, "Optical Waveguide Modeling and Design for

Evanescent Field Chemical Sensors", Opt. Quantum Electron., Vol. 26, S249-S259 (1994).

29. D. A. Stephens and P. W. Bohn, "Absorption Spectrometry of Bound Monolayers on Integrated Optical Structures", Anal. Chem., Vol. 61, No. 5, 386-390 (1989).
30. S. A. Francis and A. H. Ellison, "Infrared Spectra of Monolayers on Metal Mirrors", J. Opt. Soc. Am., Vol. 49, No. 2, 131-138 (1959).
31. N. J. Halas, I. N. Duling III, M. B. Ketchen, and D. Grischkowsky, "Measured Dispersion and Absorption of a 5 μm coplanar transmission line", CLEO Technical Digest (1986), pp.328-329.
32. R. Sprik, I. N. Duling III, C.-C. Chi, and D. Grischkowsky, "Far Infrared Spectroscopy with Subpicosecond Electrical Pulses on Transmission Lines", Appl. Phys. Lett., Vol. 51, No. 7, 548-550 (1987).
33. N. J. Harrick, "Internal Reflection Spectroscopy", Interscience, New York (1967).
34. D. L. Lee, "Electromagnetic Principles of Integrated Optics", Wiley, New York (1986).
35. H. K. V. Lotsch, "Reflection and Refraction of a Beam of Light at a Plane Interface", J. Opt. Soc. Am., Vol. 58, No. 4, 551-561 (1968).
36. R. H. Renard, "Total Reflection: A New Evaluation of the Goos-Haenchen Shift", J. Opt. Soc. Am., Vol. 54, No. 10, 1190-1197 (1964).

APPENDIX

PROOF OF EQUALITY OF $(S_{wg})_{Ray\ Optics}$ & $(S_{wg})_{Modal}$

As implied by the subscripts, $(S_{wg})_{Ray\ Optics}$ and $(S_{wg})_{Modal}$ are respectively, the sensitivities calculated using the ray optics approach and the modal field approach for the dielectric slab waveguide, when measuring the absorption of a thin dielectric film coated on one surface.

The requirement is to show that $(S_{wg})_{Ray\ Optics}$ given in Equation (6-7) and $(S_{wg})_{Modal}$ given in Equation (6-11) are mathematically identical. The proof is as follows. From the nonlinear transcendental equation (3-7),

$$\tan(\beta_{yd}h) = \frac{\alpha_{yo}\varepsilon_d}{\beta_{yd}\varepsilon_o} = \frac{\alpha_{yo}n_1^2}{\beta_{yd}} . \tag{A-1}$$

Making use of trigonometric identities along with Equation (A-1),

$$\cos^2(\beta_{yd}h) = \frac{1}{1+\tan^2(\beta_{yd}h)} = \frac{\beta_{yd}^2}{\beta_{yd}^2 + n_1^4\alpha_{yo}^2} , \tag{A-2}$$

$$\sin(2\beta_{yd}h) = \frac{2\tan(\beta_{yd}h)}{1+\tan^2(\beta_{yd}h)} = \frac{2n_1^2\alpha_{yo}\beta_{yd}}{\beta_{yd}^2 + n_1^4\alpha_{yo}^2} . \tag{A-3}$$

Substituting for $\cos^2(\beta_{yd}h)$ and $\sin(2\beta_{yd}h)$ in Equation (6-10) from Equations (A-2) and (A-3), Equation (6-11) can be written as

$$(S_{wg})_{Modal} = \frac{n_1^2 n_2 cL\left(\frac{\beta_z^2}{n_2^4} + \alpha_{yo}^2\right)\frac{\beta_{yd}^2}{(\beta_{yd}^2 + n_1^4\alpha_{yo}^2)}}{\omega\beta_z\left[h + \frac{n_1^2(\beta_{yd}^2 + \alpha_{yo}^2)}{\alpha_{yo}(\beta_{yd}^2 + n_1^4\alpha_{yo}^2)}\right]} . \tag{A-4}$$

Now, from Equation (3-5),

$$-\alpha_{yo}^2+\beta_z^2=\beta_o^2=\frac{\beta_d^2\varepsilon_o}{\varepsilon_d}=\frac{\beta_d^2}{n_1^2}. \tag{A-5}$$

Substituting for β_z in Equation (A-5) from Equation (6-2),

$$\sin^2\theta-\frac{1}{n_1^2}=\frac{\alpha_{yo}^2}{\beta_d^2}. \tag{A-6}$$

Also from Equation (3-5),

$$\frac{\beta_{yd}^2+\beta_z^2}{n_1^2}=\beta_o^2=-\alpha_{yo}^2+\beta_z^2,$$

from which it follows, $$\beta_z^2\left(1-\frac{1}{n_1^2}\right)=\frac{\beta_{yd}^2}{n_1^2}+\alpha_{yo}^2. \tag{A-7}$$

From Equation (6-4), since $n_3 = 1$,

$$\frac{t_e}{t}=\frac{4\frac{n_2}{n_1}\cos\theta\left[\frac{1}{n_2^4}\sin^2\theta+\left(\sin^2\theta-\frac{1}{n_1^2}\right)\right]}{\left(1-\frac{1}{n_1^2}\right)\left[\frac{1}{n_1^2}\sin^2\theta+\left(\sin^2\theta-\frac{1}{n_1^2}\right)\right]}. \tag{A-8}$$

Substituting for $\left(\sin^2\theta-\frac{1}{n_1^2}\right)$ from Equation (A-6) and for $\sin\theta$ from Equation (6-2),

Equation (A-8) reduces to

$$\frac{t_e}{t}=\frac{4\frac{n_2}{n_1}\cos\theta\left(\frac{\beta_z^2}{n_2^4}+\alpha_{yo}^2\right)}{\left(1-\frac{1}{n_1^2}\right)\left(\frac{\beta_z^2}{n_1^2}+\alpha_{yo}^2\right)}. \tag{A-9}$$

The denominator on the right hand side

$$\left(1-\frac{1}{n_1^2}\right)\left(\frac{\beta_z^2}{n_1^2}+\alpha_{yo}^2\right)=\frac{\beta_z^2}{n_1^2}\left(1-\frac{1}{n_1^2}\right)+\alpha_{yo}^2\left(1-\frac{1}{n_1^2}\right),$$

and substituting for $\beta_z^2\left(1-\frac{1}{n_1^2}\right)$ from Equation (A-7),

$$\left(1-\frac{1}{n_1^2}\right)\left(\frac{\beta_z^2}{n_1^2}+\alpha_{yo}^2\right)=\frac{\beta_{yd}^2}{n_1^4}+\alpha_{yo}^2\,. \qquad \text{(A-10)}$$

With the use of Equation (A-10), Equation (A-9) becomes

$$\frac{t_e}{t}=\frac{4n_1^3 n_2\cos\theta\left(\frac{\beta_z^2}{n_2^4}+\alpha_{yo}^2\right)}{\beta_{yd}^2+n_1^4\alpha_{yo}^2}\,. \qquad \text{(A-11)}$$

Substituting for Δh in Equation (6-6) from Equation (6-5), and using Equation (A-11), Equation (6-7) can be written as

$$(S_{wg})_{Ray\ Optics}=\frac{n_1^3 n_2 L\cos^2\theta\left(\frac{\beta_z^2}{n_2^4}+\alpha_{yo}^2\right)}{\sin\theta\,(\beta_{yd}^2+n_1^4\alpha_{yo}^2)\left[h\ +\ \frac{n_1^2(\beta_{yd}^2+\alpha_{yo}^2)}{\alpha_{yo}(\beta_{yd}^2+n_1^4\alpha_{yo}^2)}\right]}\,. \qquad \text{(A-12)}$$

Substituting for cos θ and sin θ from Equation (6-2), and then using $\beta_d=\frac{\omega n_1}{c}$, the term

$$\frac{n_1\cos^2\theta}{\sin\theta}=\frac{\beta_{yd}^2 c}{\omega\beta_z}\,. \qquad \text{(A-13)}$$

Combining Equations (A-12) and (A-13) yields,

$$(S_{wg})_{Ray\ Optics}=\frac{n_1^2 n_2 L\beta_{yd}^2 c\left(\frac{\beta_z^2}{n_2^4}+\alpha_{yo}^2\right)}{\omega\beta_z(\beta_{yd}^2+n_1^4\alpha_{yo}^2)\left[h\ +\ \frac{n_1^2(\beta_{yd}^2+\alpha_{yo}^2)}{\alpha_{yo}(\beta_{yd}^2+n_1^4\alpha_{yo}^2)}\right]}\,. \qquad \text{(A-14)}$$

This expression for $(S_{wg})_{Ray\ Optics}$ is identical to the one given in Equation (A-4) for $(S_{wg})_{Modal}$. Therefore, $(S_{wg})_{Ray\ Optics} = (S_{wg})_{Modal}$.